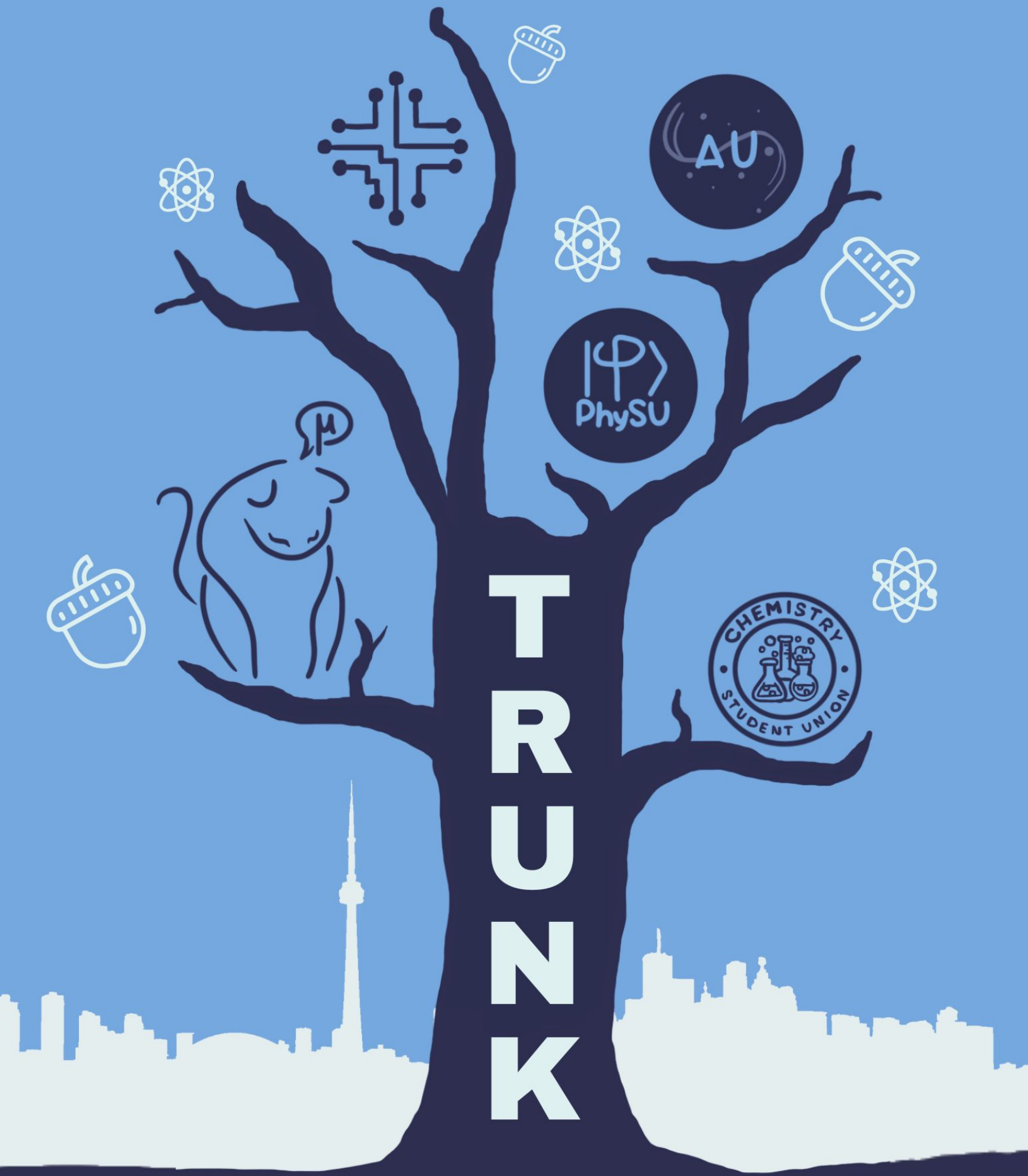


TRUNK



The UofT STEM Undergraduate Research Journal

Table of Contents

Acknowledgements	Page 2
Statement from the Organizers	Page 3
The Dynamical Properties of Stellar Streams in Cold Dark Matter and Warm Dark Matter Simulations	
Wesley Luo (Astronomy Student Union)	Page 4
Do Self-supervised Speech Models Acquire Language Bias with Regards to Phoneme Perception?	
Cynthia Sa (Computer Science Student Union)	Page 12
Preservation of Baire Spaces under Homeomorphisms	
Kai Hei Chu (Math Student Union)	Page 15
Forest Fires and Solar-induced Chlorophyll Fluorescence in Canada's Boreal Forests: Examining the Relationship of Fire Severity and Gross Primary Productivity	
Eduard K. Härtel (Physics Student Union)	Page 24

TRUNK Student Journal

Statement from the Organizers

Dear Readers,

A massive thank you to the entire team behind the first rendition of the University of Toronto's STEM Undergraduate Journal, TRUNK.

This would not be possible without our brilliant authors and editors. A congratulations to those whose papers were accepted through to the journal this year, and to those whose were not - we hope our feedback encourages you in your research careers.

This year, we had 38 'intents to submit', followed by around 11 actual submissions. Beyond this, we selected 4 of these for publication.

As a joint effort between the student unions of Computer Science, Physics, Mathematics, Chemistry, and Astronomy we hope to continue and grow this initiative in the years to come, with plans to expand our roster of subject areas each year.

Our mission is, was, and always will be to foster and advocate for undergraduate students to explore, question, and experiment to form the basis for rich experiences in research with a platform to share and present what they found or didn't find.

We hope that you enjoy reading the work of our excellent undergraduate authors, and (if you're an undergraduate at UofT yourself) that you'll consider submitting and being part of TRUNK in the future.

Regards,

The TRUNK 2024-2025 Organizing Committee

Chair: Aviraj Newatia (Computer Science Student Union)

Vice-Chair: Marty Hewitt (Physics Student Union)

Christopher Au (Chemistry Student Union)

Ishan Malhotra (Mathematics Student Union)

Melanie Szpigiel (Astronomy Student Union)

The Dynamical Properties of Stellar Streams in Cold Dark Matter and Warm Dark Matter Simulations

Wesley Luo ^{*1} Gustavo E. Medina ¹ Ting S. Li ¹ Raymond G. Carlberg ¹

Abstract

We investigate the dynamics of long, thin stellar streams in a simulated Milky Way that develops in a cold dark matter, 5.5 keV warm dark matter and 7 keV warm dark matter cosmology. Our findings reveal that the velocity dispersion of streams can be well described by a Gaussian core with exponential wings. The core's width remains relatively unaffected by the density of sub-halos, while the exponential wings vary significantly, from 2 km/s to 8 km/s depending on the dark matter cosmology. When selecting long, thin streams in galactocentric coordinates, the width of the exponential component increases as the mass of the dark matter particle increases. These results are obtained by averaging data from multiple streams, emphasizing the importance of a large sample to minimize scatter and achieve conclusive results. Our findings suggest that observational surveys with wide-field spectrographs, which can capture velocities across a stream's width, will be crucial for distinguishing between cold dark matter and warm dark matter models.

1. Introduction

A stellar stream is a narrow, elongated structure made up of stars that have been tidally stripped from a larger system, such as a dwarf galaxy or globular cluster, as it orbits a more massive galaxy like the Milky Way. In other words, these stars, once bound together, are pulled apart over time by the galaxy's tidal forces, creating a stream of stars that follows roughly the same orbit as the progenitor system. Dark matter sub-halos orbiting within a galactic halo perturb the orbits of stars in thin stellar streams (Bode et al., 2001). If dark matter particles have low thermal velocities free-

streaming effects reduce the density perturbation power (Bond and Szalay, 1983). This leads to a decrease in sub-halo numbers compared to cold dark matter (CDM) (Bode et al., 2001). Thus, viable warm dark matter (WDM) models require enough sub-halos to account for the observed dark matter-dominated dwarf galaxies in the Milky Way and nearby galaxies (Nadler et al., 2021).

Gravitational interactions between sub-halos and stellar streams are very useful in elucidating the nature of dark matter. Recent progress in this area includes constraining the radial profile of dark matter potentials using positional data of streams (Walder et al., 2024), analyzing sub-halo spreading of thin tidal streams (Carlberg and Agler, 2023), and using gaps in stellar streams to constrain the mass of the perturber dark matter sub-halo (Aganze et al., 2024).

One approach in investigating the nature of dark matter is to calculate sub-halo numbers using their effects on the radial velocity of streams. A tidal stream from a globular cluster encounters sub-halos at a rate proportional to their volume density (Carlberg, 2012). When stream stars pass through these sub-halos, their velocities change, leaving distinctive gaps in the stream over an orbital period (Carlberg, 2012). Measuring the number of these gaps as a function of size could provide information about the sub-halo mass function. However, a significant complication arises because stream stars with varying angular momenta are drawn into the stream causing internal structure to obscure and blend the gaps (Ngan et al., 2015). As gaps blend along a stream, its width and velocity dispersion become indicators of the density of dark matter sub-halos in a galactic halo. It is necessary to average the velocity profile across the entire stream since the velocity profile at a specific location along a stream may not be well mixed due to infrequent sub-halo stream interactions (Carlberg and Agler, 2023). Most known streams are relatively narrow with a high surface density, which limits their usefulness as an indicator. However, radial velocities, which can be measured accurately regardless of distance, may serve as a good indicator of sub-halo density (Carlberg and Agler, 2023).

In the following paper, we will proceed to find and characterize long, thin streams in a simulated Milky Way that develops in a cold dark matter, 5.5 keV warm dark matter

¹Department of Astronomy and Astrophysics, University of Toronto, Toronto, ON M5S 3H4, Canada. Correspondence to: Wesley Luo <wesley.luo@mail.utoronto.ca>.

ter and 7 keV warm dark matter cosmology. We will then analyze the radial velocity dispersion of these streams and discuss their merit in constraining properties of dark matter.

2. Simulation Setup

We use simulations developed by [Carlberg et al. \(2024\)](#), and will briefly describe the simulation process below. Using the MUSIC code ([Hahn and Abel, 2011](#)), a simulation of a Milky Way-like galaxy will be performed. A 40 Mpc box of dark matter particles is generated and evolved to redshift zero ([Hahn and Abel, 2011](#)). The AHF halo finder code is run on the distribution to identify Milky Way-like halos with masses near $10^{12} M_{\odot}$, with no comparable mass halos closer than 0.5 Mpc and no major mergers over the last 5 Gyr ([Gill et al., 2004](#); [Knollmann and Knebe, 2011](#)). A randomly chosen candidate halo is regenerated at much higher resolution, trimmed to fit inside a sphere and down-sampled by a factor of roughly 3.3, yielding 122,235,616 dark matter particles of mass $10,322 M_{\odot}$. The dark matter only simulation is then run from setup time to 1 Gyr before any baryonic components are inserted. At 1 Gyr, a nuclear bulge particle with mass of $5 \times 10^8 M_{\odot}$ and softening of 0.25 kpc is added. Globular clusters, made up of dynamically self-consistent $1 M_{\odot}$ star particles are also inserted. At 5 Gyr, a Miyamoto-Nagai disk-bulge centered on the nuclear bulge particle is inserted ([Miyamoto and Nagai, 1975](#)). The simulation is then run until 14 Gyr. This procedure is done three time: the first of which uses heavy cold dark matter particles and the latter two which use 5.5 keV and 7 keV warm dark matter particles. Each simulation file contains data for the positions and velocities of the cluster progenitors, stars and dark matter particles, as well as ID numbers that indicate the cluster of origin for each star.

3. Finding of Long, Thin Streams in the Simulations

Nearly every globular cluster produces a stream. Each cluster is inserted in a way that allows us to track and identify the stars belonging to it, which helps distinguish potential streams from the other particles in the simulation. These potential streams have different surface densities, widths, and lengths depending on their orbital history, and interactions. Over time, the simulated clusters have continuously lost stars to tidal streams. Stars lost long ago are dispersed throughout the halo, whereas those lost recently are found in long, thin, and dense segments. Long and thin streams are very useful since they frequently interact with sub-halos along their length and are particularly sensitive to these interactions. ([Carlberg and Agler, 2023](#)).

The analysis begins by identifying long, thin stellar streams in galactocentric coordinates using the procedure described

in Section 3.1. For each individual stream, the radial velocity dispersion is binned and fit using Equation 1. These individual dispersions are then averaged across all identified streams and similarly fit with the same equation. This process provides both individual and ensemble characterizations of radial velocity dispersion in galactocentric coordinates.

3.1. Selection of streams in galactocentric coordinates

We assume each globular cluster produces a unique stream, and to measure its properties in galactocentric coordinates, we first align the stream with its great circle coordinates (ϕ_1, ϕ_2) such that ϕ_1 is parallel to the orbit of the stream and that the center of the stream is at $(\phi_1, \phi_2) = (0, 0)$. Stream particles are placed on a grid of $0.5^{\circ} \times 0.1^{\circ}$ and smoothed with a 2D Gaussian filter of 1.5 grid elements in both directions. This procedure reveals the stream's density along its longitude.

The maximum density points along the stream are identified using latitude, radius, and three velocity components. Stream endpoints are defined where the centerline density is less than $20 M_{\odot}/\text{deg}^2$, the centerline shifts more than 2° , or any velocity component deviates by more than 30 km/s. The maximum density points are then fit with a fourth-degree polynomial to create six stream tracks shown in Figure 1. Stars within $\pm 3^{\circ}$ of this track are classified as *close stars* and are used to measure stream width and velocity dispersion. These parameters can be changed to fit any observational program.

The projected angular breadth of a stream's core is an important attribute that does not require kinematic data to be measured. A Gaussian with width σ_w has a full width at half maximum (FWHM) of roughly $2.355\sigma_w$. The FWHM for each simulated stream is determined as the $2 - \sigma$ clipped value using all close stars. Streams longer than 40° and narrower than 0.2° are classified as *long* and *thin* streams and are considered in further analysis.

3.2. Fitting radial velocity dispersion of streams

The radial velocity dispersion of long, thin streams is then plotted in a histogram with 200 bins. An example of this process is shown in Figure 2. We plot both the radial velocity dispersion of each individual long, thin stream, as well as the average dispersion of all long, thin streams. Both these histograms are fit with a function with a Gaussian core and exponential wings in the form:

$$f(v) = ae^{-\frac{1}{2}(\frac{v}{\sigma_g})^2} + be^{-\frac{|v|}{\sigma_e}} \quad (1)$$

where a and b are normalization coefficients, v is the velocity dispersion and σ_g and σ_e represent the Gaussian and exponential contributions to the dispersion respectively. σ_e

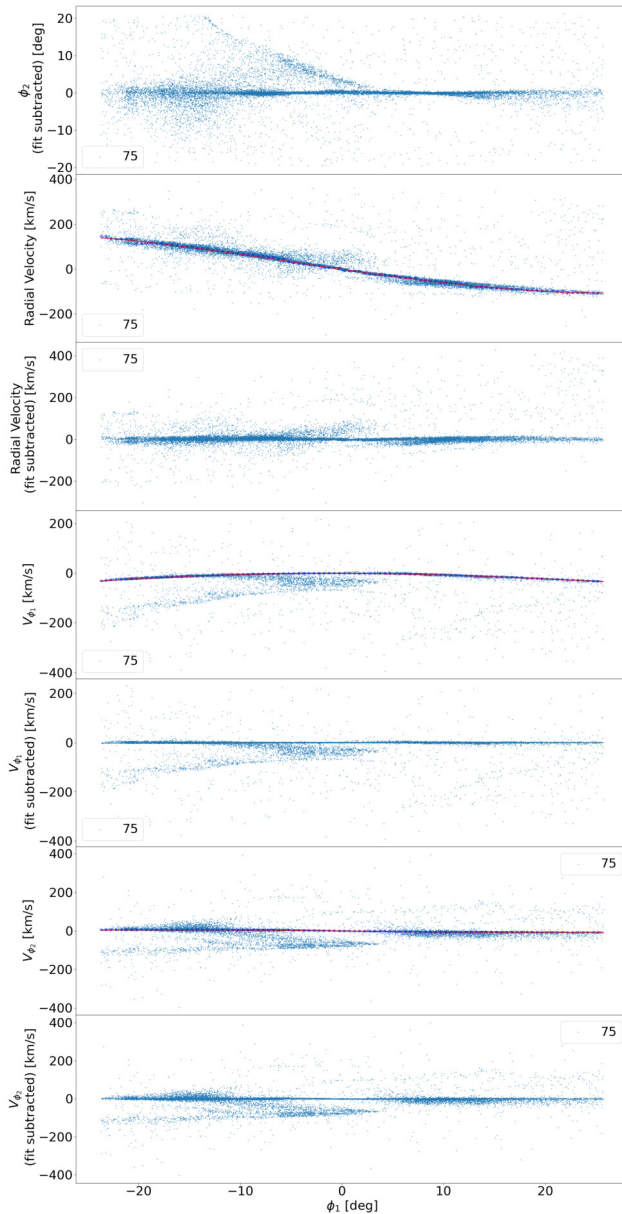
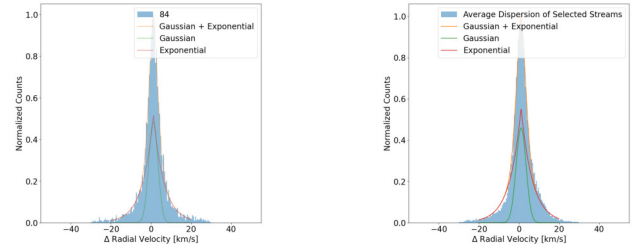


Figure 1. Stream 75 with tracks fit in 6D space. Hollow blue circles show the points the tracks are being fit to. Red lines show the stream track. Fits are being subtracted to straighten the stream which allows for easier analysis.

is a good indicator of the velocity spread of a stream which is closely correlated to the sub-halo volume density (Carlberg and Agler, 2023).



((a)) Radial velocity dispersion of stream 84 in the cold dark matter simulation when viewed in galactocentric coordinates.

((b)) Radial velocity dispersion of the average of all long, thin streams in the cold dark matter simulation when viewed in galactocentric coordinates.

Figure 2. Radial velocity dispersion of long, thin streams in the cold dark matter simulation. The initial selection of streams has been done in galactocentric coordinates. The shaded blue represents the radial velocity dispersion of the stars in the stream. The orange line represents Equation 1 which has been fit to the data. The green line represents the Gaussian portion and the red line represents the exponential portion.

4. Results

4.1. Characterization of the sample of long, thin streams selected

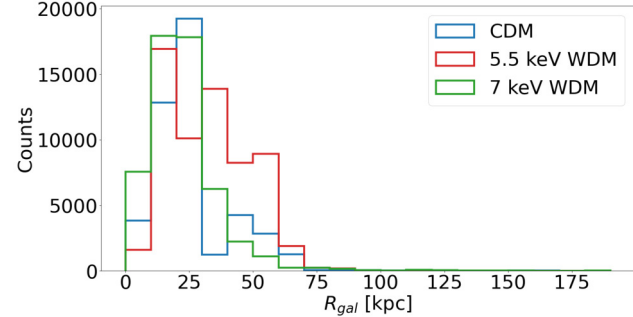


Figure 3. Galactocentric radii of the member stars of long, thin streams in the CDM, 5.5 keV WDM and 7 keV WDM simulations.

Figure 3 shows the distances of the member stars of selected streams. Stars in long, thin streams are typically found within 70 kpc of the galactic center. In the next section, we will proceed to further characterize our sample of streams by predicting how many would survive until present day and still be detectable.

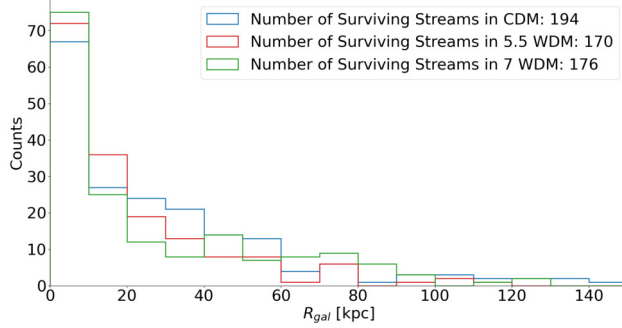


Figure 4. Surviving and detectable streams ($\Delta_0 > 2^\circ$ and $|\frac{L_z}{L}| < 0.95$) in cold dark matter (blue), 5.5 keV warm dark matter (red) and 7 keV warm dark matter simulations (green).

4.2. Surviving streams

To determine the number of surviving streams and their detectability, we will employ the method used in (Pearson et al., 2024) which involves calculating two quantities:

1. Streaminess Δ_0
2. Z-fraction of angular momentum $|\frac{L_z}{L}|$

The streaminess quantity is defined as

$$\Delta_0 = \sqrt{\text{med}(l)^2 + \text{med}(b)^2} \quad (2)$$

and is indicative of how phase mixed a stream is. For streams with $\Delta_0 \approx 0$, the debris is dispersed close to the bulge region of the Milky Way or fully phase mixed around the center (Pearson et al., 2024). The other quantity $|\frac{L_z}{L}|$ is the fraction of angular momentum contained in the z-component. Streams with $|\frac{L_z}{L}| \approx 1$ solely rotate in the disk which makes them very difficult to detect (Pearson et al., 2024). We classify surviving and detectable streams as those with $\Delta_0 > 2^\circ$ and $|\frac{L_z}{L}| < 0.95$. Shown in Figure 4 is the distribution of surviving and detectable streams. We find 194, 170 and 176 surviving streams in the cold dark matter, 5.5 keV warm dark matter and 7 keV warm dark matter simulations respectively. In (Pearson et al., 2024), they found over 500 surviving streams in each of their Milky Way simulations. However, their simulations did not include the effects of dark matter sub-halos on these streams. Including these effects would reduce the number of surviving streams since most streams would experience sub-halo perturbations which would make some of them fail the streaminess criteria (Ngan et al., 2015).

4.3. Stream properties

Shown in Figure 5 is the σ_e and σ_g scatter when fitting the radial velocity dispersion of long, thin cold dark matter streams. The same process has been repeated for the 5.5

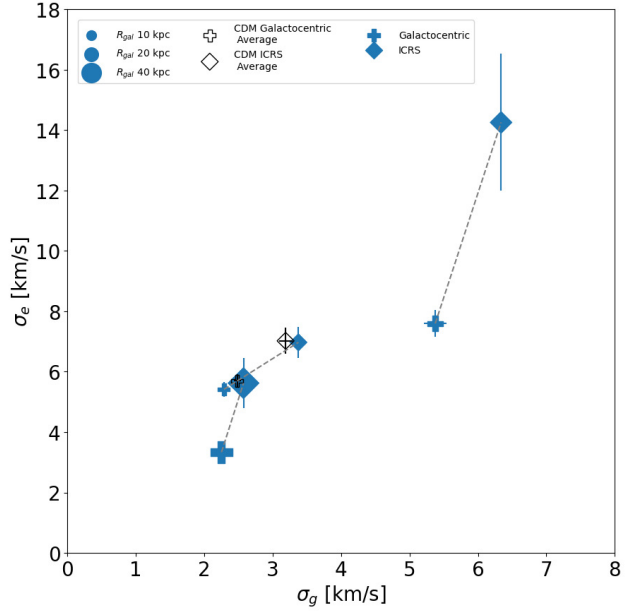


Figure 5. Scatter in σ_e and σ_g of long, thin streams in the cold dark matter simulation. The values for σ_e and σ_g of the same stream in a different coordinate system are connected by a dotted gray line. The marker size indicates the galactocentric radii of the progenitor of the stream.

keV and 7 keV warm dark matter streams and the results are shown in Figures 6 and 7. The selected long, thin stellar streams are also transformed into the International Celestial Reference System (ICRS), which positions the observer at the location of the Sun, thereby emulating the observational perspective of real astronomical data.

In the cold dark matter simulation, we find very few long, thin streams. The properties of the individual streams also tend to change a lot depending on the coordinate system.

As for the 5.5 keV warm dark matter simulation shown in Figure 6, we see much less scatter than in the cold dark matter simulation.

For the 7 keV warm dark matter simulation (Figure 7), aside from a single outlier, there is minimal variation in σ_e and σ_g observed between the different coordinate systems.

For all dark matter cosmologies (cold dark matter, 5.5 keV warm dark matter, 7 keV warm dark matter), averaging σ_e and σ_g across multiple streams yields consistent results regardless of the coordinate system.

4.4. Constraining mass of dark matter particle

The average σ_e values are plotted against their respective dark matter particle mass in Figure 8. The average values of σ_e show a clear correlation with the mass of the dark matter

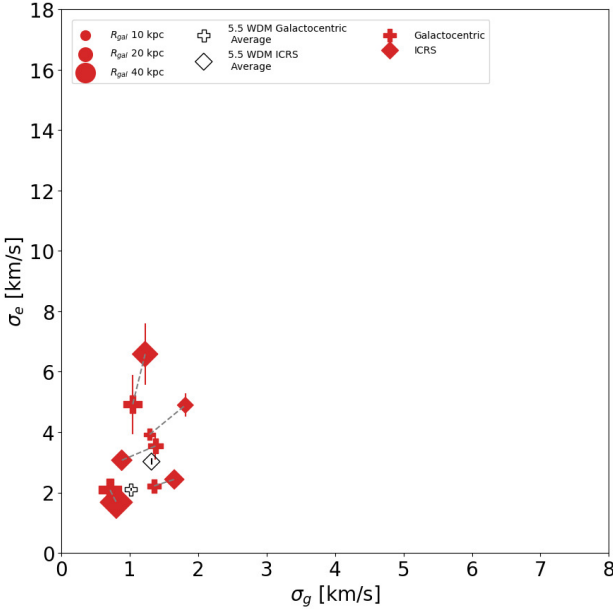


Figure 6. Scatter in σ_e and σ_g of long, thin streams in the 5.5 keV warm dark matter simulation. The values for σ_e and σ_g of the same stream in a different coordinate system are connected by a dotted gray line. The marker size indicates the galactocentric radii of the progenitor of the stream.

particle. This is expected, as a heavier dark matter particle supports the formation of a larger number of massive sub-halos, leading to increased perturbations and, consequently, higher velocity dispersion in stellar streams (Carlberg and Agler, 2023). The values for σ_e in the ICRS coordinate system are significantly lower than those in the galactocentric coordinate system. This is due to most of the velocity dispersion being seen in the tangential and perpendicular components instead of the radial component (Figures 9, 10, 11).

5. Discussion

We predict that there are many potential streams that could be detected today. Long, thin streams would probably be found within 70 kpc of the galactic center which means that we do not need to look into the outskirts of the Milky Way to find these streams. A large sample of streams is needed when performing analysis since lots of scatter is present when analyzing individual streams. Additionally, the correlation between radial velocity dispersion and the mass of the dark matter particle is better seen in galactocentric coordinates. Since the radial component of velocity is easier to measure than the parallel and perpendicular components, analysis should be done in galactocentric coordinates.

For streams viewed in ICRS coordinates, the velocity dispersion spread (σ_e) is more prominent in the parallel and

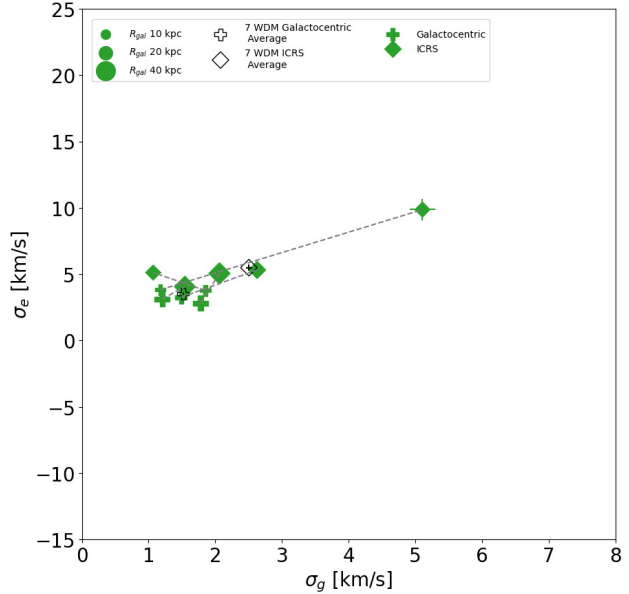


Figure 7. Scatter in σ_e and σ_g of long, thin streams in the 7 keV warm dark matter simulation. The values for σ_e and σ_g of the same stream in a different coordinate system are connected by a dotted gray line. The marker size indicates the galactocentric radii of the progenitor of the stream.

perpendicular components rather than the radial component. This is the most noticeable for cold dark matter streams as seen in Figure 8. Obtaining parallel and perpendicular velocity components is observationally challenging, as it requires precise proper motion measurements and accurate distance estimates which is especially difficult in the distant halo. In contrast, the radial component is relatively straightforward to measure using Doppler shifts in stellar spectra.

The radial velocity dispersion of long, thin streams differs significantly between cold dark matter and warm dark matter simulations when the initial selection is done in galactocentric coordinates. A model with a Gaussian core and exponential wings is a good fit for the velocity distributions. The Gaussian core is only slightly affected by the density of sub-halos. However, the width of the exponential wings varies from 2 km/s to 8 km/s as seen in Figures 5, 6 and 7.

To ensure a consistent result, the radial velocity dispersions in the study are averaged among numerous streams ranging from three to twelve. In a cold dark matter cosmology, few sub-halo-stream interactions cause large velocity shifts, resulting in significant differences in the velocity dispersion profiles between streams depending on their interaction histories. Therefore, it is necessary to average the radial velocity dispersion profiles from multiple streams to achieve a stable result. Although there are few major sub-halo interactions, resulting in poor mixing of velocities at any particular location along the stream, the overall velocity distribution

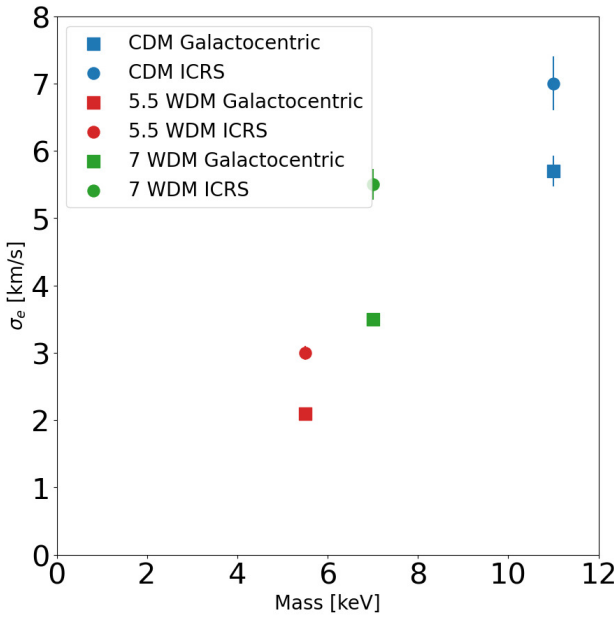


Figure 8. Exponential fit parameter of the radial velocity dispersion (σ_e) against mass of dark matter particle for various dark matter cosmologies.

function across the whole length of the stream is reasonably smooth. Current large-scale spectroscopic surveys may acquire a high number of velocities over a significant width around a few streams, allowing for a conclusive measurement. Additional simulations examining a variety of Milky Way-like assembly histories and a larger spectrum of globular cluster mass distributions would be beneficial in guiding future observational studies.

6. Conclusion

In this paper, we examined the dynamics of long, thin stellar streams in a simulated Milky Way that developed in a cold dark matter, 5.5 keV warm dark matter and 7 keV warm dark matter cosmology. Our results indicate that there may exist a large population of surviving stellar streams within $R_{\text{gal}} < 80$ kpc. We found that analyzing long, thin streams in galactocentric coordinates, rather than ICRS coordinates, is more effective for constraining dark matter properties. Maintaining the analysis in galactocentric coordinates ensures consistency with simulations and reveals a clearer correlation between the radial velocity dispersion (σ_e) and the dark matter particle mass. These findings suggest that characterizing the radial velocity dispersion profiles of such streams in galactocentric coordinates may be a particularly promising approach for probing the nature of dark matter.

References

- Christian Aganze, Sarah Pearson, Tjitske Starkenburg, Gabriella Contardo, Kathryn V. Johnston, Kiyan Tavangar, Adrian M. Price-Whelan, and Adam J. Burgasser. Prospects for Detecting Gaps in Globular Cluster Stellar Streams in External Galaxies with the Nancy Grace Roman Space Telescope. , 962(2):151, February 2024. doi: 10.3847/1538-4357/ad159c.
- Paul Bode, Jeremiah P. Ostriker, and Neil Turok. Halo Formation in Warm Dark Matter Models. , 556(1):93–107, July 2001. doi: 10.1086/321541.
- J. R. Bond and A. S. Szalay. The collisionless damping of density fluctuations in an expanding universe. , 274: 443–468, November 1983. doi: 10.1086/161460.
- R. G. Carlberg. Dark Matter Sub-halo Counts via Star Stream Crossings. , 748(1):20, March 2012. doi: 10.1088/0004-637X/748/1/20.
- Raymond G. Carlberg and Hayley Agler. Subhalo Spreading of Thin Tidal Star Streams. , 953(1):99, August 2023. doi: 10.3847/1538-4357/ace4be.
- Raymond G. Carlberg, Adrian Jenkins, Carlos S. Frenk, and Andrew P. Cooper. Star stream velocity distributions in cold dark matter and warm dark matter galactic halos. *The Astrophysical Journal*, 975(1):135, oct 2024. doi: 10.3847/1538-4357/ad7b35. URL <https://dx.doi.org/10.3847/1538-4357/ad7b35>.
- Stuart P. D. Gill, Alexander Knebe, and Brad K. Gibson. The evolution of substructure - I. A new identification method. , 351(2):399–409, June 2004. doi: 10.1111/j.1365-2966.2004.07786.x.
- Oliver Hahn and Tom Abel. Multi-scale initial conditions for cosmological simulations. , 415(3):2101–2121, August 2011. doi: 10.1111/j.1365-2966.2011.18820.x.
- Steffen R. Knollmann and Alexander Knebe. AHF: Amiga’s Halo Finder. *Astrophysics Source Code Library*, record ascl:1102.009, February 2011.
- M. Miyamoto and R. Nagai. Three-dimensional models for the distribution of mass in galaxies. , 27:533–543, January 1975.
- E. O. Nadler, A. Drlica-Wagner, K. Bechtol, S. Mau, R. H. Wechsler, V. Gluscevic, K. Boddy, A. B. Pace, T. S. Li, M. McNanna, A. H. Riley, J. García-Bellido, Y. Y. Mao, G. Green, D. L. Burke, A. Peter, B. Jain, T. M. C. Abbott, M. Aguena, S. Allam, J. Annis, S. Avila, D. Brooks, M. Carrasco Kind, J. Carretero, M. Costanzi, L. N. da Costa, J. De Vicente, S. Desai, H. T. Diehl, P. Doel, S. Everett, A. E. Evrard, B. Flaugher, J. Frieman,

D. W. Gerdes, D. Gruen, R. A. Gruendl, J. Gschwend, G. Gutierrez, S. R. Hinton, K. Honscheid, D. Huterer, D. J. James, E. Krause, K. Kuehn, N. Kuropatkin, O. Lahav, M. A. G. Maia, J. L. Marshall, F. Menanteau, R. Miquel, A. Palmese, F. Paz-Chinchón, A. A. Plazas, A. K. Romer, E. Sanchez, V. Scarpine, S. Serrano, I. Sevilla-Noarbe, M. Smith, M. Soares-Santos, E. Suchyta, M. E. C. Swanson, G. Tarle, D. L. Tucker, A. R. Walker, W. Wester, and DES Collaboration. Constraints on Dark Matter Properties from Observations of Milky Way Satellite Galaxies. , 126(9):091101, March 2021. doi: 10.1103/PhysRevLett.126.091101.

Wayne Ngan, Brandon Bozek, Raymond G. Carlberg, Rosemary F. G. Wyse, Alexander S. Szalay, and Piero Madau. Simulating Tidal Streams in a High-resolution Dark Matter Halo. , 803(2):75, April 2015. doi: 10.1088/0004-637X/803/2/75.

Sarah Pearson, Ana Bonaca, Yingtian Chen, and Oleg Y. Gnedin. Forecasting the Population of Globular Cluster Streams in Milky Way-type Galaxies. *arXiv e-prints*, art. arXiv:2405.15851, May 2024. doi: 10.48550/arXiv.2405.15851.

Madison Walder, Denis Erkal, Michelle Collins, and David Martínez-Delgado. Probing the dark matter haloes of external galaxies with stellar streams. In *EAS2024*, page 1695, July 2024.

A. Appendix

In this section of the Appendix, we show the dispersion in all three velocity components for each long, thin stream. In Figures 9, 10 and 11, we show the velocity dispersion profiles along all three components as well as the stream width profile for streams in the warm dark matter simulations.

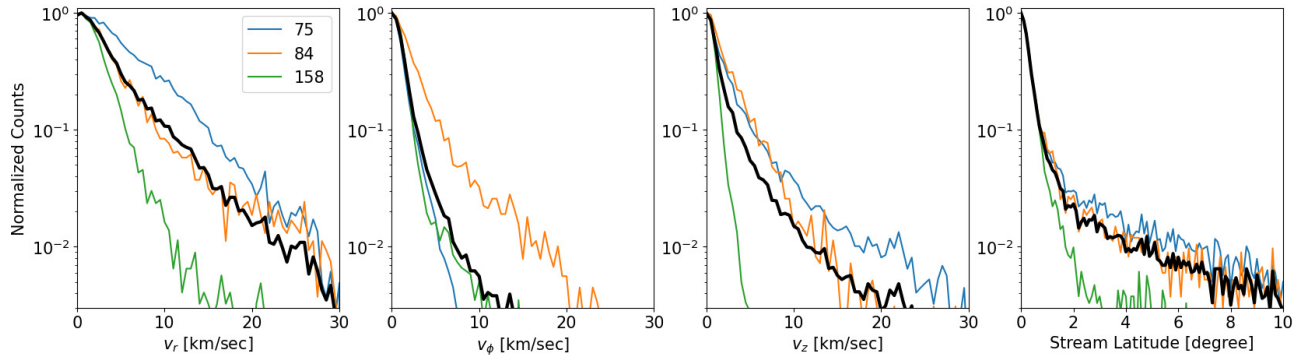


Figure 9. Radial, parallel and perpendicular velocity and stream width dispersion of each long, thin stream selected in the cold dark matter simulation.

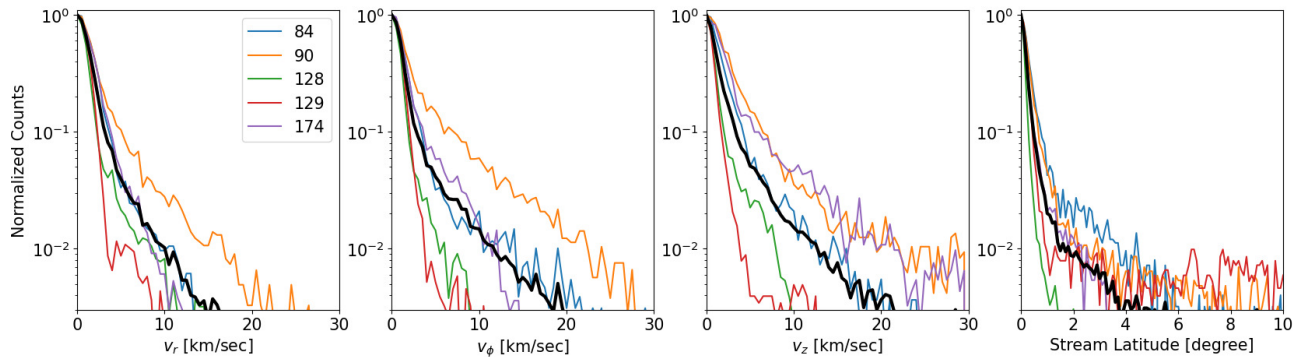


Figure 10. Radial, parallel and perpendicular velocity and stream width dispersion of each long, thin stream selected in the 5.5 keV warm dark matter simulation.

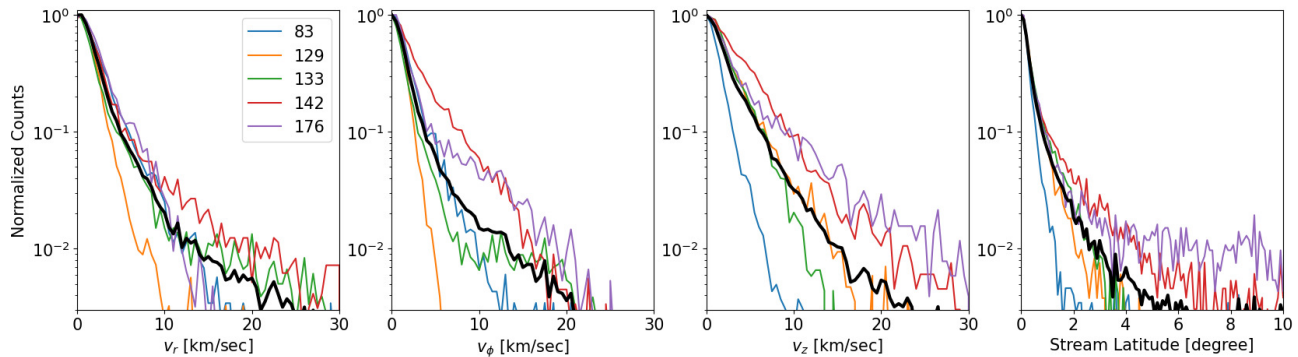


Figure 11. Radial, parallel and perpendicular velocity and stream width dispersion of each long, thin stream selected in the 7 keV warm dark matter simulation.

Do self-supervised speech models acquire language bias with regards to phoneme perception?

Cynthia Sa

University of Toronto

Toronto, Canada

cynthia.sa@mail.utoronto.ca

Abstract—Deep self-supervised learning models of speech do not learn from explicit textual labels and are very flexible in deriving speech representations from unlabelled data. Research has shown that these self-supervised learning models learn speech representations that correlate with linguistic categories, such as phonemes. Interestingly, absorbing phoneme categories through exposure to speech mirrors how infants acquire these categories during language learning. Given this parallel, would these models of speech be similarly effective in discriminating between unfamiliar phoneme categories? If so, this would imply that self-supervised speech models inherit language bias with regards to phoneme perception based upon the speech used in its training. In this paper, we analyze phoneme-level properties in the learned representations of two popular models - HuBERT and wav2vec2.0 - through comparison with human participant performance in phoneme discrimination trials using speech from unfamiliar languages. Recent studies have also shown that iteration significantly impacts models' learned representations and their correlation to linguistic categories. We further explore how iterative refinement affects learned speech representations and whether it strengthens perceptual biases when disambiguating between phoneme categories. We find a strong and stable correlation between the phoneme discrimination accuracy of both human participants and the speech models, suggesting that HuBERT and wav2vec2.0 develop language bias with regards to phoneme perception, and iterative refinement further magnifies this effect.

I. INTRODUCTION

Self-supervised deep learning models of speech have proven to be highly effective in many applications, such as speech recognition and speaker identification [2]. The high performance self-supervised learning models have on these downstream tasks has invited studies regarding what types of information are encoded by the models, and to what extent. Analysis by Pasad, Chou, and Livescu [3] of the wav2vec2.0 model demonstrates that the model encodes phone identity, word identity, and to a lesser extent, word meaning and local acoustic features. They also found that wav2vec2.0 experiences a significant drop in correlation with all aforementioned linguistic units in its representations as it approaches its final layers. The HuBERT model, while encoding similar linguistic categories, does not experience the same drop in correlation in its learned representations. Recent work by Huo [1] compared the difference between the framework of these two models and found that iterative refinement, not objective, caused the main difference in linguistic correlations between the two models. We seek to further investigate how these models of speech

encode phoneme-level information in their representation by comparing speech representations of pre-trained models to the results of human participants in an ABX vowel discrimination task, analyzing how the relationship between these two measures evolves across layers, and how the correlation is altered when iterative refinement is used. In this work, we will be focusing our analysis on the open-source HuBERT model and a minimally modified base HuBERT model that has been pretrained with wav2vec2.0's contrastive loss objective. This minimally modified base HuBERT model is used in place of wav2vec2.0's open-source model to explore the impact of multiple training iterations on the model and its learned representations.

II. BACKGROUND

Comprehensive work has already been done in analyzing both the information encoded in these self-supervised learning models of speech and what aspects of their framework influence the extent to which this information is preserved in their representations.

Previous work by Pasad, Chou, and Livescu [3] made use of canonical correlation analysis (CCA) to explore what information the wav2vec2.0 model encoded, and how the information encoded evolved throughout the layers. Canonical correlation analysis (CCA) is a statistical technique used as a measure of similarity to compare representations within and across neural network models, deriving the relationship between two continuous-valued random vectors as represented by the maximum correlations between their linear projections. Pasad, Chou, and Livescu [3] computed CCA correlation with phoneme and word identity for representations from each layer of the wav2vec2.0, and subsequently observed that wav2vec2.0 experienced a notable drop in its correlation with linguistics units in its representations from the final layers.

To further investigate this phenomenon, Huo [1] compared the framework of wav2vec2.0 to that of HuBERT, a similar model which had no drop in its correlation from the final layers. Both models shared the same encoder architecture and creation of pseudo-labels masked prediction through clustering the output. However, there were several important differences. Most critically, HuBERT used multiple training iterations whereas wav2vec2.0 did not. To explore the impact that iterative refinement may have on the information encoded by these models, they minimally modified the base HuBERT model

to pretrain it with wav2vec2.0's contrastive loss objective. This adjusted model was analogous to wav2vec2.0 but with iterative refinement. They trained both the model analogous to wav2vec2.0 and a base HuBERT model for two iterations each, and performed CCA correlation with phoneme and word identity for representations from each layer of the models. As a result, they found that both models in their first iterations experienced a drop in correlation, matching prior results to wav2vec2.0. In contrast, both models in their second iteration had small or no such CCA decrease in their final layers, matching previous results found for the HuBERT model. This suggests that iteration has a strong impact on the encoded linguistic correlations in these self-supervised learning models of speech.

III. METHODS

We make use of a set of human behavioural data derived from an ABX discrimination task performed on monolingual French and English participants [2]. In this task, the set of stimuli used was constructed of recorded CVC (consonant-vowel-consonant) audio from languages that were unfamiliar to the participants. The participant would hear both a "target" stimulus and an "other" stimulus, not necessarily in that order, then finally a stimulus "X," which always belonged to the same vowel phone category as the target stimulus. The target stimulus and the other stimulus would at all times be vowels that are both present in one of multiple languages. The purpose of this ABX task was to measure how effectively participants were able to discriminate between unfamiliar speech sounds. Stimulus triplets that more participants could correctly identify "X" as belonging to "target" were recorded as easier for these participants to discriminate, and vice versa. Participants also indicated a degree of certainty in their own answers between 1, 2, and 3 in the order of increasing certainty. For the purposes of this analysis, we made use of the resulting gradient dependent measure, wherein a scale of 3, 2, 1 indicated correct answers of decreasing certainty, and -3, -2, -1 indicated incorrect answers of decreasing certainty. This additional measure captures more information than the otherwise binary result of an ABX task, allowing us to take into account the confidence participants had when undergoing the task. The use of the gradient offers us increased statistical power and reduces any reliance on aggregating across trials. In this paper, we are examining the results of monolingual English-speaking participants.

With the results of the ABX Discrimination task, we group by and subsequently average the scale dependent measure across unique vowel contrast pairs, irrespective of order. The resulting value is our **human accuracy score**, or the average confidence and correctness that English participants had when discriminating between the two vowels in that pair.

Following the research of Huo [1], we tested a HuBERT model with a classification loss objective, and a minimally modified HuBERT model pretrained with wav2vec2.0's contrastive loss. Both of these models have 12 layers. These two models were trained on public-domain English audio books from the LibriSpeech corpus.

With each model and each of their layers, we extract a representation for M for each of the stimuli making up each target/other/X triplet within the experiment. Following this, we compute a Δ -value for each triplet (target/other/X) used in a trial with an English-speaking participant:

$$\Delta = DTW(M_{\text{other}}, M_x) - DTW(M_{\text{target}}, M_x)$$

Here, DTW is the distance obtained by using dynamic time warping to aggregate the frame-level cosine distance along the warping path. We further normalized the result according to the length of each stimulus or the number of frames that comprise each representation, resulting in a Δ that measures the model's ability to discriminate between the target and other phone categories. The greater the Δ -value, the more similar the learned representation of X is to the target's representation, and the more dissimilar X's representation is to the representation of the other. This implies that the model would classify X as being more similar to the target, allowing us to calculate a measure that allows comparison between the model's representations and the results of the ABX discrimination task.

To compare the human accuracy score with our model's representations, we take the participant's discrimination task average within each contrast pair and the average of each model layer's Δ -values, and use **Spearman's correlation**. The resulting values illustrate how similar a certain model perceives unfamiliar phones to be, in comparison to the average human participant's perception of these same unfamiliar speech sounds.

IV. RESULTS

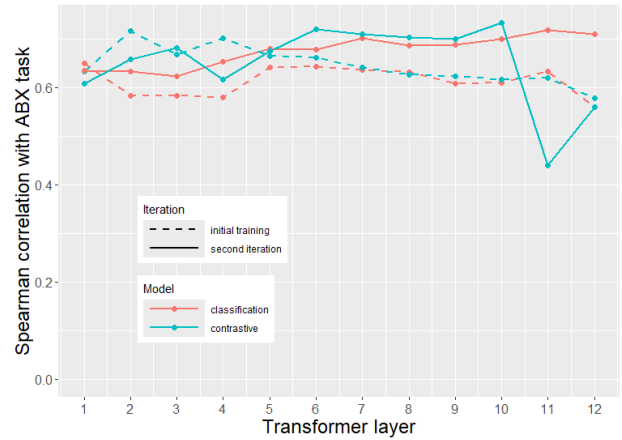


Fig. 1. Spearman correlation with ABX discrimination task results of 1st-iteration contrastive model (analogous to wav2vec2.0) and 2nd-iteration classification model (standard HuBERT).

The results of this analysis are shown in Fig. 1, and the results of the previous work of Robin et al. [2] are depicted in Fig. 2. In general, the models show some similar behaviours between the human accuracy correlation and the CCA correlation results. In both trials, the models improved

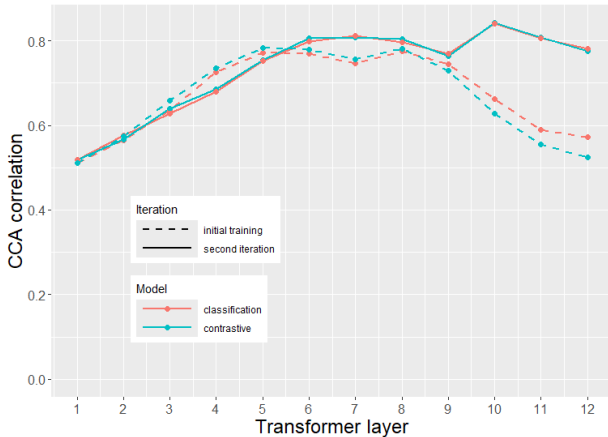


Fig. 2. CCA results of 1st-iteration contrastive model (analogous to wav2vec2.0) and 2nd-iteration classification model (standard HuBERT), derived from data by Huo [1].

significantly in stability and accuracy in their second iteration compared to their first. In their first iterations, they tend to be lower correlated to the human accuracy score and CCA, with a small preference for the wav2vec2.0 (contrastive objective) model within the first five layers. In their second iteration, the correlation score for both models grows significantly higher and presents as a more steady increasing correlation.

In prior work, both models had very similar performances to one another in their first and second iterations [1]. In our trial, we note more significant differences between the two. The wav2vec2.0 (contrastive objective) model demonstrated a rather unstable trend in both the first and second iterations, with the first iteration presenting a general downward trend and the second iteration presenting a general upward trajectory but a sharp decline at the 10th layer. The HuBERT model (classification objective) comparatively is much more stable throughout both iterations. In its second iteration, it has a lower correlation to the human accuracy score than the wav2vec2.0 model but remains much more steady in its upward trend and remains so throughout all layers.

In analyzing these results, we note three main observations. These graphs present much more clearly that there is a definitive and noticeable impact made by objective. Unlike the results depicted from Huo [1], the final results between the two models are not mirrored in the first and second iterations - they are notably different with a slight reliability preference to the HuBERT model or classification objective.

All correlation values in general stay in a limited range surrounding 0.6, denoting that they are all presenting rather similar correlation values. From this, we can assume that while there is an important difference between iteration and objective, both models perform at about the same level of correlation to human accuracy as the other. In these results, a more consistent distance between the results of the first and second iteration can also be seen. At layers 5 and 7, the wav2vec2.0 model demonstrates the same correlation value between both iterations. Otherwise, in both models, there is

a consistent gap that remains across most of the layers. In comparison to past results [1], Fig. 2 demonstrates that in contrast, the CCA correlation values were very weak from the beginning layer in both models. The gap between both iterations in their results is also much larger and much less consistent across layers.

V. DISCUSSION

Through the high correlations demonstrated, we have shown that self-supervised speech models have developed some degree of language bias with regards to phoneme perception, aligned with what has been observed in English participants' results across several phoneme discrimination tasks. While throughout the layers, the behaviour of our models is generally increasing its correlation with the human accuracy score, some patterns denote it is far from a perfect relationship or correlation. For instance, there is a noticeable instability seen in the trend for the wav2vec2.0 or contrastive objective model. This, and its other subsequent differences in pattern compared to the HuBERT model, can be likely attributed to their difference in objective. While it is difficult to say how exactly the difference in objective between contrastive and classification has led to the patterns seen in our results, our work does offer a definitive new perspective on how these two models make use of linguistic categories through their speech representations.

Regarding iterative refinement, it strengthened the correlation between the human accuracy score and both the HuBERT and wav2vec2.0 models. In prior research by Huo [1] which can also be seen in Fig. 2, the second iteration models were significantly more CCA correlated. Our results show a different trend in the second iteration. A possible explanation is that the new target label clusters the models have begun to use as a result of iterative refinement are inclined towards phoneme categories specific to the language they have been trained upon. We speculate that the model not only develops some degree of language bias with regards to phoneme perception but that this bias is magnified through iterative refinement.

REFERENCES

- [1] Robin Huo. "Influence of training objective and iterative training on the linguistic information encoded by self-supervised neural models of speech".
- [2] Juliette Millet and Ewan Dunbar. "Do self-supervised speech models develop human-like perception biases?" In: *Proceedings of the 60th Annual Meeting of the Association for Computational Linguistics (Volume 1: Long Papers)*. 2022, pp. 7591–7605. DOI: 10.18653/v1/2022.acl-long.523. URL: <https://aclanthology.org/2022.acl-long.523/>.
- [3] Ankita Pasad, Ju-Chieh Chou, and Karen Livescu. "Layer-wise analysis of a self-supervised speech representation model". In: *2021 IEEE Automatic Speech Recognition and Understanding Workshop (ASRU)*. IEEE. 2021, pp. 914–921.

Preservation of Baire Spaces under Homeomorphisms

Author: Kai Hei (Clement) Chu

Abstract

We aim to study the preservation of Baire properties under homeomorphisms. The key results will be established with the aid of major theorems like the Baire Category Theorem, as well as key properties of homeomorphisms. Applications of such results include invariance of Baire property under finite compositions of homeomorphisms, and its preservation in complete metric spaces.

Introduction

This paper focuses primarily on a particular class of topological spaces known as Baire spaces. Along the way, we will introduce concepts such as metric spaces, topologies, open dense sets, and major theorems like the Baire Category Theorem to help us build intuition toward our main goal: understanding the preservation of Baire structures under homeomorphisms, and when it could be applied.

One might have seen in a standard topology course that, even though the preimage of open sets under a continuous map is open, their image is not necessarily always open. This motivates us to ask the central question: what structures are well-preserved under certain maps, in particular, homeomorphisms? The focus on Baire spaces is also far from arbitrary. Many important spaces, such as complete metric spaces, are indeed Baire spaces. Moreover, Baire spaces are very well preserved under homeomorphisms, although properties like completeness are not well preserved under them.

While several claims of this paper could be proven directly by definition, our objective is to present an alternative, more elegant approach to this topic. Specifically, we will connect theorems like the Baire Category Theorem with metric and topological spaces and homeomorphic mappings, demonstrating the complex interplay between different fields. Moreover, it will be revealed later that the proofs of some key results are conceptually a lot cleaner and elegant using this approach.

1. PRELIMINARY DEFINITIONS

Definition 1.1 (Metric Spaces): Given a set X , a metric space on the set X with the distance function $d : X \times X \rightarrow \mathbb{R}$ by (X, d) , that has the following properties:

- $\forall x, y \in X, d(x, y) \geq 0$
- $\forall x, y \in X, d(x, y) = 0 \Leftrightarrow x = y$
- $\forall x, y \in X, d(x, y) = d(y, x)$
- $\forall x, y, z \in X, d(x, z) \leq d(x, y) + d(y, z)$

Definition 1.2 (Topology): A topology on a set X is a collection, denoted as \mathcal{T} , of open subsets of X that satisfies the following properties:

- $\emptyset \in \mathcal{T}$ and $X \in \mathcal{T}$
- The arbitrary union of sets in \mathcal{T} is also in \mathcal{T} . That is, $\bigcup_{i \in I} X_i \in \mathcal{T}$, where $X_i \in \mathcal{T}$ and I is an indexing set
- The finite intersection of sets in \mathcal{T} is also in \mathcal{T} . That is, $\bigcap_{i=1}^n X_i \in \mathcal{T}$, where $X_i \in \mathcal{T}$

Definition 1.3 (Open ball on a metric space): Let $\varepsilon > 0$. Let (X, d) be a metric space. The *open ball*, centered at a point x in a set X with radius ε , is denoted as $B_\varepsilon(x)$, where $B_\varepsilon(x) = \{y \in X : d(x, y) < \varepsilon\}$

2. BAIRE SPACES

Definition 2.1 (Open sets): A set X is open if $\forall x \in X, \exists \varepsilon > 0$ such that $B_\varepsilon(x) \subseteq X$.

More generally, in a topological space (X, \mathcal{T}) , the open sets are simply the elements of the topology.

Definition 2.2 (Density): A set X is dense in Y if $\forall y \in Y, \forall \varepsilon > 0, B_\varepsilon(y) \cap X \neq \emptyset$. More generally, in a topological space (X, \mathcal{T}) , $A \subseteq X$ is dense if and only if $\forall U \in \mathcal{T}, U \neq \emptyset \implies A \cap U \neq \emptyset$.

Motivations

In the metric space (\mathbb{R}, d) , where d is the standard Euclidean metric, one can easily show that the finite union of open and dense sets of metric space is open and dense. An example would be, for all $\varepsilon > 0$, the set $(-\varepsilon, \varepsilon) \cup \mathbb{Q}$ is dense because each of $(-\varepsilon, \varepsilon)$ and \mathbb{Q} is dense.

This raises a crucial question: Is the *countable* intersection of open dense sets dense as well? This naturally leads to the notion of Baire spaces, where it perfectly addresses this concern, as presented in the next section.

However, before we prove such claim, it is crucial to define what a complete metric space is.

Definition 2.4 (Complete Metric Space): A metric space (X, d) is said to be *complete* if every Cauchy sequence in X has a limit that is also in X .

Here, we would provide a brief introduction to what a *Sorgenfrey line* is. The Sorgenfrey line is a topological space denoted by $(\mathbb{R}, \mathcal{T}_S)$, where $S = \{[a, b] : a, b \in \mathbb{R}\}$ and \mathcal{T}_S is a topology on \mathbb{R} generated by the basis S . We shall first present a brief proof outline of the claim that the Sorgenfrey line is **not** metrizable, meaning there is no metric for this topology. It serves as a bit of counter-intuitive example for later sections.

Proposition 2.5: The *Sorgenfrey line* is not metrizable.

Proof Outline: One common approach to prove that it is not metrizable by *Urysohn's metrization theorem*, meaning every second countable space is metrizable. For clarity we would omit the proof. One can show that the Sorgenfrey line is not second countable hence using the theorem, we can show that it is not metrizable. (See Khatchatourian[5]) \square

Lemma 2.6: A finite intersection of open sets in a metric space is open.

Proof: Let $M = (X, d)$ be an arbitrary metric space with distance function d . Let S_i be open subsets of M . Let $S = \bigcap_{i=1}^n S_i$ be the finite intersection of the open subsets. Fix an arbitrary point $x \in S$. Since $x \in S$, x must be in each of S_i , for $i \in \{1, \dots, n\}$. Since each of the S_i are open, by definition, for each of the S_i , there exists a $\varepsilon_i > 0$ such that $B_{\varepsilon_i}(x) \subseteq S_i$. Let $\varepsilon = \min\{\varepsilon_1, \dots, \varepsilon_n\}$. It is immediate that $B_{\varepsilon_i}(x) \subseteq B_\varepsilon(x)$, for each of $i \in \{1, \dots, n\}$. Thus, $B_\varepsilon(x) \subseteq B_{\varepsilon_i}(x) \subseteq S_i \subseteq S$. Since x was chosen arbitrarily, for all x in S , there exists an $\varepsilon > 0$ such that $B_\varepsilon(x) \subseteq S$. By definition, S is open. \square

Theorem 2.7: A countable intersection of open dense sets of a complete metric space is dense.

Proof: Let $M = (X, d)$ be an arbitrary, complete metric space. Let U_1, U_2, \dots be open dense sets in M . We shall denote its countable intersection as $S = \bigcap_{i=1}^{\infty} U_i$. Fix $\varepsilon > 0$. We want to show that $\forall x \in M, B_\varepsilon(x) \text{ such that } B_\varepsilon(x) \cap S \neq \emptyset$.

By assumption, since U_1 is an open dense set, by *definition 2.2*, we know that $\forall x \in X, \forall \varepsilon > 0, B_\varepsilon(x) \cap U_1 \neq \emptyset$. Equivalently, there exists an element $u_1 \in U_1$ such that $u_1 \in B_\varepsilon(x)$. By *lemma 2.6*, we know that the intersection $B_\varepsilon(x) \cap U_1$ is also open. Thus, there exists an $0 < \varepsilon_1 < \frac{1}{2}$ such that $\overline{B_{\varepsilon_1}(u_1)} \subseteq B_\varepsilon(x) \cap U_1$ (By *definition 2.1*). Notice that we can do the same for U_2 , that is, by *lemma 2.6*, by the fact that $B_{\varepsilon_1}(u_1) \cap U_2$ is open, there exists an $0 < \varepsilon_2 < \frac{1}{4}$ such that $\overline{B_{\varepsilon_2}(u_2)} \subseteq B_{\varepsilon_1}(u_1) \cap U_2$ for some element $u_2 \in U_2$. We repeat this for all of U_i , for $i \in \{1, 2, \dots\}$. By doing this iteratively, we have produced both a sequence of points u_i as well as a sequence of radius ε_i , for $i \in \{1, 2, \dots\}$.

We claim that the sequence of points $u_n = \{u_i\}_{i=1}^{\infty}$ is Cauchy in X . That is, we want to show that, for all $n, m > N$, $d(u_n, u_m) < \varepsilon$. Choose a value N such that $\frac{1}{2^N} < \frac{\varepsilon}{2}$. Observe that, $B_{\varepsilon_{n+k}}(x) \subseteq B_{\varepsilon_n}(x)$, for any $k \in \mathbb{N}$. Thus, it must be true that for all $n, m > N$, u_n and u_m , to lie in the ball $\overline{B_{\varepsilon_N}(u_N)}$. Thus, $d(u_n, u_N) < \frac{1}{2^N}$ and $d(u_m, u_N) < \frac{1}{2^N}$. By triangle inequality, $d(u_n, u_m) \leq d(u_n, u_N) + d(u_m, u_N) < \frac{1}{2^N} + \frac{1}{2^N} < \frac{\varepsilon}{2} + \frac{\varepsilon}{2} = \varepsilon$. By definition, u_n is a Cauchy sequence. We now use the assumption that the metric space is complete. Since it is a complete metric space, notice that by *definition 2.4*, the limit of u_n must also be in (X, d) . Let the limit

point be s .

Since each of $\overline{B_{\varepsilon_N}(u_N)}$ is closed, it must contain all its limit points. It follows that s must also be contained in each of the $\overline{B_{\varepsilon_n}(u_n)}$ for $n \in \mathbb{N}$. Notice $\overline{B_{\varepsilon_n}(u_n)} \subseteq B_{\varepsilon_{n-1}}(u_{n-1}) \cap U_n \subseteq U_n$ and $\overline{B_{\varepsilon_n}(u_n)} \subseteq B_{\varepsilon_{n-k}}(u_{n-k})$ for any $k \in \mathbb{N}$. It must then be true that $\overline{B_{\varepsilon_n}(u_n)} \subseteq B_{\varepsilon_1}(u_1) \subseteq B_{\varepsilon}(x)$. Also, s is in $\overline{B_{\varepsilon_N}(u_N)}$, so $s \in U_n$ and $s \in B_{\varepsilon}(x)$ for $n \in \mathbb{N}$. We have now showed that $s \in \bigcap_{n=1}^{\infty} U_n \cap B_{\varepsilon}(x)$, so $B_{\varepsilon}(x) \cap S \neq \emptyset$. This completes the proof by the definition of denseness. \square

Definition 2.8 (Baire Space): A topological space X that satisfies the condition where countable intersection of open dense sets is dense is called a Baire space.

This is a phenomenal result, and the result of *theorem 2.7* is known as 'Baire Category Theorem'. An immediate consequence is as below:

Corollary 2.9: If X is a complete metric space, then X is a Baire space.

Proof: The proof follows immediately from *theorem 2.7*, since countable intersection of open dense sets of a complete metric space is dense, which is by definition a Baire space. \square

We shall take some time and revisit the example with *Sorgenfrey line*, which the introduction in *Proposition 2.5* may seem initially unmotivated. We showed that since the Sorgenfrey topology on \mathbb{R} is so "fine" in a sense that the basis of the topology is generated by intervals of the form $[a, b)$, the real line equipped with the topology generated by such basis would be not metrizable. We might think that intuitively, since Baire spaces are mostly these nice metric spaces, as shown in *Corollary 2.9*, the Sorgenfrey line should not be a Baire space. However, we will see that it is.

Proposition 2.10: The Sorgenfrey line is a Baire space.

Proof Outline: Define the Sorgenfrey line as the topological space $(\mathbb{R}, \mathcal{T}_S)$. Here, similar to the construction as before, $S = \{[a, b) : a, b \in \mathbb{R}\}$, and \mathcal{T}_S is the topology on \mathbb{R} generated by the basis S . Let the collection of open dense set in the topology be denoted as $\{U_n\}_{n=1}^{\infty}$. We will proceed by the definition of denseness. We want to show that for all open dense sets $A \supseteq [a, b)$ in the topology (Since $[a, b)$ is a basis so it generates A), $[a, b) \cap (\bigcap_{n=1}^{\infty} U_n) \neq \emptyset$.

Fix an interval $[a, b)$. Since U_1 is dense, we construct an interval $[x_1, y_1) \subseteq [a, b) \cap U_1$ since by definition, $[a, b) \cap U_1 \neq \emptyset$. We would then construct another interval, again by definition of denseness, such that $[x_2, y_2) \subseteq [x_1, y_1) \cap U_2$. Repeating this process iteratively, we construct a sequence of intervals such that $[x_n, y_n) \subseteq [x_{n-1}, y_{n-1}) \cap U_n$. Notice that the intervals are shrinking such that the final interval left would contain one point, which is the supremum over the set of x_i . Let such point be denoted as p . First, $p \in [x_n, y_n) \subseteq [x_{n-1}, y_{n-1}) \cap U_n \subseteq U_n$. But by construction of p , $p \in \bigcap_{n=1}^{\infty} [x_n, y_n) \subseteq \bigcap_{n=1}^{\infty} [x_{n-1}, y_{n-1}) \cap U_n \subseteq \bigcap_{n=1}^{\infty} U_n$. Also, p is in $[a, b)$ since $p \in [x_n, y_n) \subseteq [x_{n-1}, y_{n-1}) \cap U_n \subseteq [x_n, y_n) \dots \subseteq [x_1, y_1) \subseteq [a, b)$. p is in both $[a, b)$ and $\bigcap_{n=1}^{\infty} U_n$, so $[a, b) \cap (\bigcap_{n=1}^{\infty} U_n) \neq \emptyset$. It then follows by definition that it is a Baire space. \square

3. HOMEOMORPHISMS AND MOTIVATIONS

We now begin our study towards the most important results of this paper, which is to discover the preservation of Baire structures under homeomorphic mappings.

Definition 3.1 (Homeomorphisms): Let X and Y be topological spaces. A map $\varphi : X \rightarrow Y$ is said to be a homeomorphism if:

- φ is continuous
- φ is bijective
- Its inverse, φ^{-1} is continuous

Example 3.2: A simple example of a homeomorphism would be the identity map on any topological space. \square

WHY CONSIDER BAIRE SPACES?

Before we dive even further, it is reasonable to question the motivation behind proving the relationship between Baire spaces and homeomorphisms. Although homeomorphisms have many nice properties that we would explore later in the subsequent lemmas since they are isomorphisms in the category of topological spaces, it is not always true that homeomorphisms preserve the properties like, completeness of a metric space. As an example, it is simple to show that there exists a homeomorphism between \mathbb{R} and also the open interval $(0,1)$, however, notice that \mathbb{R} is complete while $(0,1)$ is unfortunately, not. We will however, in later proofs, show that it does preserve the structure of Baire Spaces, which is a very nice property to have since density is well preserved.

As promised, we shall now start exploring the properties in which homeomorphisms preserve.

Note: In what follows, a topological space (X, \mathcal{T}) , where \mathcal{T} is a topology on the set X , would be denoted as X when the topology is well understood from context.

Lemma 3.3: Let X_1, X_2 be topological spaces. Let $\varphi : X_1 \rightarrow X_2$ be a homeomorphism. If $U \subseteq X_1$ is an open dense set, then $\varphi(U) \subseteq X_2$ is an open dense set.

Proof: First, by the definition of homeomorphisms, since φ^{-1} and φ are continuous and are bijective, we know that $\varphi(U)$ is open. It is now left to prove that, for any non-empty open sets $V \subseteq X_2$, $V \cap \varphi(U) \neq \emptyset$. Since φ is bijective, $V \cap \varphi(U) = \varphi(\varphi^{-1}(V) \cap U)$. We know that under a continuous inverse, $\varphi^{-1}(V)$ is open. Notice that by assumption, U is dense, thus $\varphi^{-1}(V) \cap U \neq \emptyset$. (This holds true since φ is bijective). Then, the image $\varphi(\varphi^{-1}(V) \cap U)$ is non-empty. So, $\varphi(\varphi^{-1}(V) \cap U) = V \cap \varphi(U) \neq \emptyset$, which is precisely what we want to show. \square .

Lemma 3.4: Let X_1, X_2 be topological spaces. Let $\varphi : X_1 \rightarrow X_2$ be a homeomorphism. If $V \subseteq X_2$ is an open dense set, then $\varphi^{-1}(V) \subseteq X_1$ is an open dense set.

Proof: The proof of this lemma closely mirrors the proof of lemma 3.3, so it is omitted. \square

Lemma 3.5 Let X_1, X_2 be topological spaces. If $\varphi : X_1 \rightarrow X_2$ is a homeomorphism, then $\varphi^{-1} : X_2 \rightarrow X_1$ is a homeomorphism.

Proof: We assume φ is a homeomorphism. Thus, φ^{-1} is continuous and bijective. Also, it is continuous by the definition of homeomorphism. Thus, φ^{-1} is a homeomorphism. \square

These are just a few of the structures that homeomorphisms preserve. We would now shift our attention to our final goal. That is, the preservation of Baire structures under homeomorphic mappings.

Theorem 3.6: Let X, Y be topological spaces. Let $\varphi : X \rightarrow Y$ be a homeomorphism. Then, X is a Baire space if and only if Y is a Baire space.

Proof: We assume X is a Baire space. Our goal is to prove that Y is a Baire space. Let $\{U_n\}_{n=1}^{\infty}$ be a collection of open dense sets in Y . First, the inverse φ^{-1} exists since φ is a homeomorphism. By *lemma 3.4* we know that $\varphi^{-1}(U_n)$ is open and dense. Hence, by the assumption that X is a Baire space, $\bigcap_{n=1}^{\infty} \varphi^{-1}(U_n)$ must be dense in X by definition. Thus, since φ is a homeomorphism, $\varphi(\bigcap_{n=1}^{\infty} \varphi^{-1}(U_n))$ is dense by *lemma 3.3*, and using the fact that φ is bijective, $\bigcap_{n=1}^{\infty} U_n$ is dense in Y . Therefore, Y is a Baire space. The other direction follows by replacing φ by φ^{-1} . \square

We shall now see some powerful, elegant applications of this theorem. Also notice that our previous results would lead to remarkably concise proofs for the following corollaries.

Corollary 3.7: The image of a complete metric space X under a homeomorphism φ is a Baire space.

Proof: If X is a complete metric space, then by *corollary 2.9*, X is a Baire space. By *theorem 3.6*, Y must also be a Baire space since φ is a homeomorphism. \square

Corollary 3.8: Let X be a Baire space. Let Y be a space that is homeomorphic to X and Z be a space that is homeomorphic to Y . Then, Z is a Baire space.

Proof: The proof follows directly from *theorem 3.6*. Since, if Y is homeomorphic to X , and X is a Baire space, then Y is a Baire space by *theorem 3.6*. Then, if Z is homeomorphic to Y , then applying *theorem 3.6* again, Z must be a Baire space. \square

In functional analysis, *Theorem 3.6* could also well connect to spaces like Banach spaces. A Banach space is a complete normed vector space. Normed meaning that it is equipped with the norm metric (similar to the Euclidean norm in the Euclidean space), and complete by *Definition 2.4*. Using *Theorem 3.6*, if X is a Banach space and is homeomorphic to another space, say Y , then Y must also be a Baire space. Even though it might not be a Banach space, it preserves the nice properties of Baire spaces, via structure-preserving maps such as homeomorphisms.

This is one of many possible impacts it may have on areas like functional analysis, topology, differential equations, ergodic theory and much more, demonstrating its utility in many different fields.

Acknowledgment

The idea of this template is based from "Template artigo TCC IC-UFF (Bacharelado em Sistemas de Informação - SI)", used under the terms of Creative Commons CC BY 4.0.

References

1. Durrani, Asad. *MAT327, Lecture 1*, University of Toronto, May 8 2019.
<https://www.math.toronto.edu/ivan/mat327/docs/lecturenotes/lecture1-AsadDurrani.pdf>
2. Hadfield, Andrew. *Handout 7*. University College London, 2010.
<https://www.ucl.ac.uk/ucahad0/3103handout7.pdf>.
3. Ilia. *MAT378, Metric Spaces*, University of Toronto, 2010.
<https://www.math.utoronto.ca/ilia/Teaching/MAT378.2010/Metric20Spaces.pdf>
4. Khatchatourian, Ivan. *MAT327, 06-Continuity*, University of Toronto, 2018.
<https://www.math.utoronto.ca/ivan/mat327/docs/notes/06-continuity.pdf>
5. Khatchatourian, Ivan. *MAT327, 12-Metric Spaces*, University of Toronto, 2018.
<https://www.math.utoronto.ca/ivan/mat327/docs/notes/12-metric.pdf>

Forest Fires and Solar-induced Chlorophyll Fluorescence in Canada's Boreal Forests: Examining the Relationship of Fire Severity and Gross Primary Productivity

Eduard K. Härtel, Supervisor: Prof. Debra Wunch^a

^a*Earth, Atmospheric and Planetary Physics Group, University of Toronto*

Abstract

I examined burn severity and the recovery of photosynthetic activity for twenty-one large wildfires ($>100,000$ ha) in Canada's boreal region between 2010 and 2015. The research objectives were: 1) to use a remotely-sensed Solar-Induced chlorophyll Fluorescence (SIF) indicator to approximate Gross Primary Productivity (GPP) recovery, and 2) to characterize post-fire photosynthesis recovery relative to initial fire severity using GPP. Advances in the use of SIF measurements to approximate GPP at moderate temporal and spatial resolutions, along with land cover analysis to account for variations in the SIF-GPP relationship by land cover type, provided the foundation for this research. Before the fires (in 2009), land cover was dominated by evergreen needleleaf forests. In 2019 (four to nine years after the fires), the median land cover showcased a significant decrease in high density evergreen needleleaf forests and an increase in herbaceous, shrubby, and grassy cover. I correlated between five and ten years of post-fire recovery rates (until 2020) to fire severity, which ranged from 400 to 600 (as indicated by the delta Normalized Burn Ratio, dNBR), and tracked overall recovery rates as a function of recovery years. For all fires, a weak inverse relationship could be seen between SIF recovery and severity ($r = -0.27$). Similarly, a weak inverse relationship was determined between GPP or carbon uptake and severity ($r = -0.27$). It took roughly 6 years after the initial fire for the analyzed fire areas to make a full recovery to a 5-year pre-fire mean SIF and a little less than 7 years for GPP to recover fully.

Keywords: Remote Sensing, Solar-induced Chlorophyll Fluorescence, Carbon Fluxes, Fire Severity

1. Introduction

The 2023 fire season was the most severe in Canada's recorded history [26]. It will likely not be the last season of such extremes, with temperatures similar to those of 2023 expected frequently over the next decades [4]. Since roughly 60% of Canada's land area is covered with boreal forest [27], wildfire disturbances that influence the carbon cycle of the boreal forest have a significant impact on Canada's greenhouse gas emissions. In the past two decades, Canadian forests have released more carbon than they have absorbed [11] - and with climate change bringing hotter temperatures, emissions from Canada's boreal forest are expected to rise further in the future [1].

The 2023 season alone would offset national emissions targets by more than 10 years [46] with emissions on managed land so severe, they outsized annual budgets of every country aside from the US, China and India [4]. This was also a crucial factor in contributing to 2023 being the weakest land sink since 2003 globally [21]. Emissions of such magnitude can severely affect Canada's national greenhouse gas inventory, which it agreed to maintain along with net-zero commitments in the Paris Agreement [43, 5], but these emissions are currently unaccounted for. Despite explicitly lobbying for an inclusion of carbon sinks in national greenhouse gas inventories in 2001 [8], Canada pulled out of

the Kyoto Agreement when compliance costs became too high [35]. Canada currently does not include any wildfire emissions in its nationally determined contributions to the Paris Agreement [44]. This exclusion is justified by the claim of only accounting for anthropogenic sources of carbon [11]. But there is growing pressure on the inclusion of such emissions into the national greenhouse gas inventory, since the IPCC identifies all emissions on managed lands as anthropogenic [4]. A renewed inclusion would have significant implications on Canada's economy and environmental governance as Canada's lands are turning from sinks to sources. Even under the current accounting scheme, Canada is not on track to meet its targets with existing and planned policies [6]. Increasing wildfire emissions would thus further undermine Canada's ability to adhere to its Paris commitments.

With stronger fire seasons influencing global land sinks and potentially having monumental impacts on national greenhouse gas accounting, it is crucial to examine how Canada's boreal carbon fluxes respond to fires, and how they might recover emitted carbon. Recent studies have aimed to understand how forest carbon fluxes might change based on post-fire vegetation succession [23], pyrogenic carbon remaining after fires [20], and CO₂ fertilization from an increased atmospheric carbon concentration [22, 1]. However, little research

has been conducted on the relationship between fire severity and carbon flux [23] despite studies suggesting climate change may be increasing fire severity [34] and affecting post-disturbance forest recovery [17], signaling growing urgency.

Although current measures adequately represent over-story burn severity - the degree of wildfire damage on the canopy - detecting changes in understory burn severity may require alternate remote sensing metrics [17]. And while some research has been conducted on the relationship of fire severity and carbon uptake [34], and a recent study related GPP to fire severity [18], so far only vegetation indices have been used to analyze this relationship. While reflectance-based greenness vegetation indices work fairly well with deciduous trees, shrubs, and grasses, evergreen needleleaf forests will not exhibit strong seasonal fluctuations in greenness that can be traced using a vegetation index - despite reducing photosynthetic activity in winter [19]. To fill this knowledge gap, this paper aims to identify the recovery of Solar-induced chlorophyll fluorescence (SIF) as a proxy for Gross Primary Production (GPP) in Canadian boreal forest areas after fires of varying severity. This pilot study will offer a blueprint for a more thorough analysis of the relationship between fire severity and post-fire photosynthesis recovery.

Solar-Induced chlorophyll Fluorescence (SIF) refers to the near-infrared light emitted by chlorophyll molecules within leaves during photosynthesis. After absorbing photosynthetically active radiation (PAR) from sunlight within the visible spectral range (approximately 400 to 700 nm wavelength), the chlorophyll becomes excited, and the energy can follow three main pathways: photochemistry (used for photosynthesis), non-photochemical quenching as heat, or fluorescence emitted as light [9]. Most of the absorbed energy is directed toward photochemistry, but a fraction of around 1% is emitted as fluorescence [3]. Recent advancements in remote sensing have enabled this radiation to be measurable from space through the in-filling of Fraunhofer lines - narrow absorption features in the solar spectrum where the sun's atmosphere absorbs sunlight and prevents it from reaching the Earth regardless of the Earth's atmospheric composition [9]. By examining Fraunhofer lines near the Oxygen A-band (around 720 nm wavelength), we can measure the fractional depth filled by fluorescence photons to find SIF and estimate photosynthetic activity with greater accuracy than previously possible [14, 9]. This has significant implications for analyzing the carbon cycle, as SIF serves as a reliable proxy for assessing photosynthetic processes across various biomes over a large spatial scale [14]. Gross Primary Production (GPP) is the total amount of carbon dioxide that is assimilated by vegetation through photosynthesis over a specific period, and thus synonymous with photosynthetic activity [3]. As one of the largest components in the terrestrial ecosystem and carbon budget, its balance with ecosystem respiration -

the release of carbon dioxide through plant metabolism - determines net ecosystem exchange (NEE) [47], which plays a pivotal role in whether our natural environment is a carbon sink or storage, ameliorating or exacerbating the carbon dioxide buildup in the atmosphere. The accurate measurement of GPP is thus crucial to understanding the forest carbon cycle and the contribution of NEE to atmospheric carbon dioxide [49]. Traditionally, in situ measurements have been used to estimate GPP, but these methods are limited in spatial coverage [48]. Remote sensing techniques thus offer a promising alternative, allowing for a continuous monitoring of GPP across large areas.

Studies have demonstrated that SIF can be effectively used to estimate GPP, revealing a linear relationship across ecosystems, but especially throughout North America's boreal forests and on a monthly scale [40, 23]. This relationship is underpinned by the understanding that both SIF and GPP derive from the same source of energy – average photosynthetically active radiation absorbed by chlorophyll [48]. Gross primary production (GPP, $\text{gC m}^{-2} \text{ s}^{-1}$) is linearly related to solar-induced chlorophyll fluorescence (SIF, $\text{W m}^{-2} \text{ sr}^{-1} \text{ nm}^{-1}$) through the equations:

$$\text{GPP} = \varepsilon_{\text{LUE}} \times \text{APAR} \times f(T) \times f(P) \quad (1)$$

$$\text{SIF} = \varepsilon_F \times \varepsilon_{\text{ESC}} \times \text{APAR} \quad (2)$$

$$\text{GPP} = \frac{\varepsilon_{\text{LUE}}}{\varepsilon_F \times \varepsilon_{\text{ESC}}} \times \text{SIF} \quad (3)$$

where ε_{LUE} (gC mol^{-1}) is the light-use efficiency, ε_F is the fluorescence yield, ε_{ESC} is the escape fraction of fluorescence, APAR ($\text{mol m}^{-2} \text{ s}^{-1}$) is the absorbed photosynthetically active radiation, and $f(T)$ and $f(P)$ are stress factors that account for temperature and precipitation dependencies - constants respectively [32].

Using SIF data can thus allow us to estimate GPP and enhance the understanding of carbon cycling in the context of disturbances such as wildfires. But with slight differences in the slope of the GPP/SIF linear relationship depending on plant functional type [23], it will be important to examine how land cover change might affect the recovery rate when correlating severity and GPP.

This paper will leverage SIF data to explore how post-fire carbon uptake recovery times vary with fire severity, ultimately providing insights into the boreal forest's resilience and carbon sequestration potential. By seeking to determine how the sequestration capabilities of Canada's boreal forests might be affected by fire severity, this work is in line with Goal 10 of the 2023 Blueprint for Forest Carbon Science in Canada: better understanding and predicting natural disturbance regimes in a changing climate, and impacts on carbon pools, transfers, and fluxes [36].

In the first section of this paper, I review the utilized datasets and the reasoning behind their use. The next two sections thoroughly review the data and methods used for the analysis. After showcasing the results, the

findings are interpreted and limitations and uncertainties discussed - providing an outlook on possible future research foci.

2. Data

2.1. Canadian National Fire Database (CNFDB)

Fire information was retrieved from the Canadian National Fire Database, an annually updated database compiled and maintained by the Canadian Forest Service in cooperation with provincial, territorial, or Parks Canada fire management agencies under Natural Resources Canada [29, 29]. For each recorded fire on managed lands in Canada, it records the agency in charge, a fire identifier, temporal information, size, and the cause of the fire. This information is stored in a shapefile, which also contains the fire location point data and fire perimeter polygons. The dataset was chosen for its completeness and cross-identification capability, since the unique fire IDs recorded in the CNFDB match those in the CanLaBS severity product.

2.2. Canada Landsat Burned Severity (CanLaBS)

The fire severity was retrieved from Landsat 5, 7 and 8 satellites, which record images in a range of spectra, and was consolidated in the Canada Landsat Burned Severity (CanLaBS) product [17]. This dataset spans from 1985 to 2015 and records the severity of the latest fire at 30m resolution over any given area. This was a good fit for the observed fire timeframe from 2010 to 2015.

Fire severity was estimated using the difference in normalized burn ratios (dNBR) by comparing pre-fire and post-fire measurements. The Normalized Burn Ratio (NBR) is an index designed to highlight burnt areas in large fire zones using both near infrared (NIR) and shortwave infrared (SWIR) wavelengths. While healthy vegetation shows a very high reflectance in the NIR and low reflectance in the SWIR portion of the electromagnetic spectrum (Figure 1), burnt areas demonstrate low reflectance in the NIR and high reflectance in the SWIR. This difference primarily arises from a change in water content in the reflecting material. Healthy vegetation holds water that absorbs radiation in the SWIR spectrum, whereas charcoal has far less water content, reflecting light in the SWIR [33]. NBR is determined by the normalized difference between NIR and SWIR:

$$NBR = \frac{NIR - SWIR}{NIR + SWIR} \quad (4)$$

A high NBR value therefore indicates healthy vegetation while a low value indicates bare ground and recently burnt areas [17]. The more vegetation is replaced by char, the greater this spectral response difference will be, and thus the dNBR will greater. This dataset was chosen since it provides a median dNBR for each fire region and aligns with fire IDs provided in

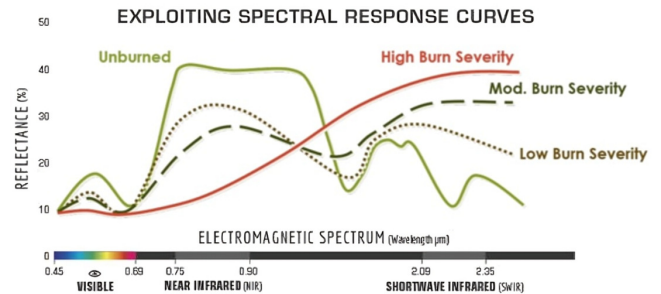


Figure 1: Comparison of the spectral response of healthy vegetation and burned areas. Adapted from: [25], [45]

the CNFDB. DNBR was calculated by [17] by differencing pre-fire NBR with post-fire NBR: For post-fire years with cloud coverage, which applied to roughly 8% of fires, a linear regression was used from non-cloudy post-fire years to conduct a radiometry correction.

2.3. Contiguous Solar-induced Fluorescence

I used the global spatially contiguous solar-induced chlorophyll fluorescence dataset (CSIF) generated with clear-sky training data from the SIF-measuring satellite Orbiting Carbon Observatory-2 (OCO-2) from 2015 and 2016 [48]. OCO-2 is on a sun-synchronous orbit, allowing it to take measurements daily at the same time for each region it passes. But with a limited swath of just 10 km, it only revisits the same location roughly every 2 weeks. This means the data it collects has fairly large gaps in between swaths, as can be seen in the top image of Figure 2 which shows measurements for an entire month. To create contiguity, Zhang's CSIF product used surface reflectance data from the Moderate-resolution Imaging Spectroradiometer (MODIS) aboard NASA's Terra and Aqua satellites as input variables [48]. For the years 2000–2020, four bands of 0.05°-resolution nadir bidirectional reflectance distribution adjusted reflectance (MODIS MCD43C4) were used to approximate SIF. These were selected because they contain most of the vegetation information related to the variation of SIF. Through the use of Neural Network inference connecting input and training variables, the researchers then created a spatially continuous dataset of SIF values.

After training, the CSIF product was validated with SIF data from OCO-2 for 2014 and 2017, and GOME-2, an earlier satellite from 2007 to 2013, which has a broader spatial resolution at 960km but a lower spectral resolution [2].

The CanLaBS dataset was chosen due to its unique contiguity over the Canadian boreal region, and its comparatively fine temporal resolution. It also covered the years 2000 to 2020, giving a sufficient temporal breadth to study pre- and post-fire trends. At a 0.5° resolution or ca. 50 km x 50 km, the dataset is also fairly accessible in terms of size, making it operable with limited computational resources.

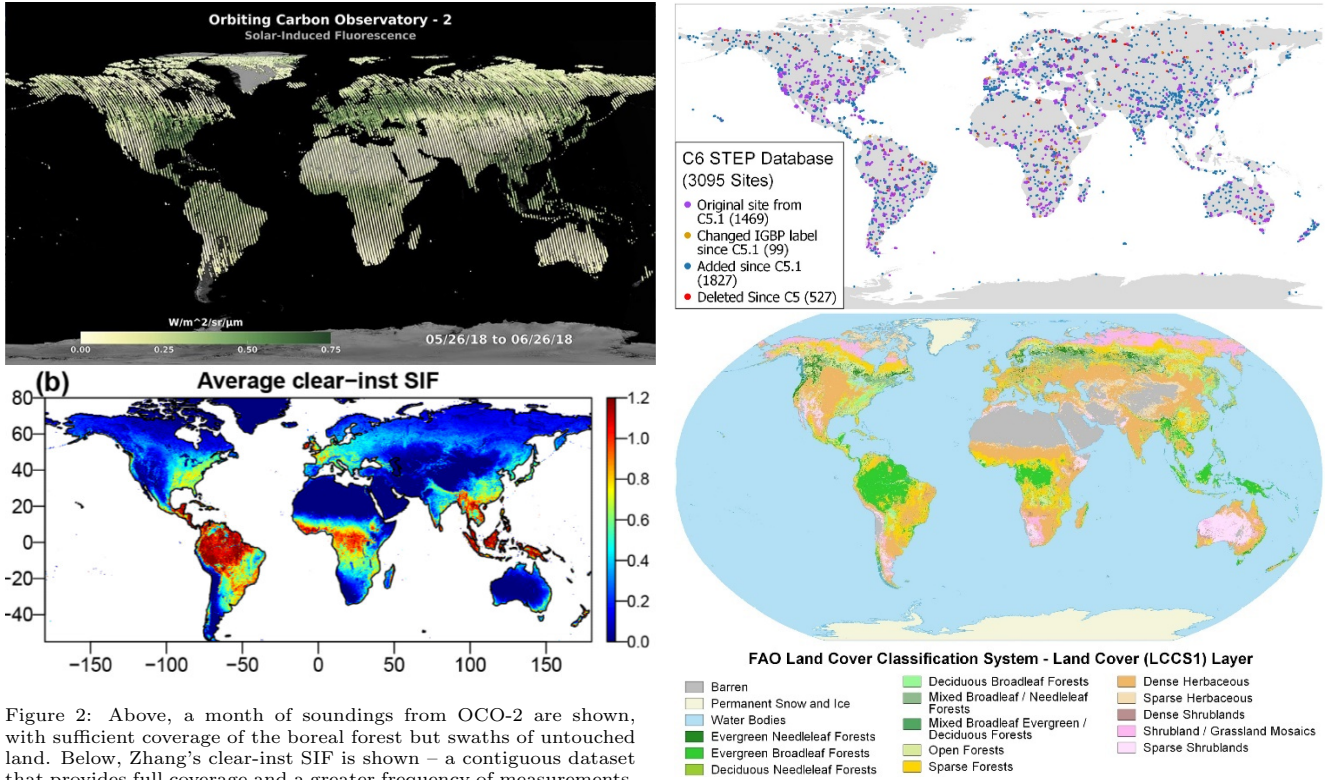


Figure 2: Above, a month of soundings from OCO-2 are shown, with sufficient coverage of the boreal forest but swaths of untouched land. Below, Zhang's clear-inst SIF is shown – a contiguous dataset that provides full coverage and a greater frequency of measurements. Sources: [31, 48]

One risk of using this dataset stems from its dependence on MODIS NBAR reflectance data, making it only an approximation of SIF with some uncertainty. While it is a better proxy for GPP than reflectance-based measurements, it is not as accurate as a direct SIF measurement. Uncertainties are further compounded by technical difficulties OCO-2 experienced in August and September of 2017, leading to lower coverage in boreal region validation data [48].

2.4. MODIS Land Cover Type (MCD12Q1)

Land cover information was drawn from MODIS MCD12Q1v061 which referenced the UN Food and Agricultural Organization (FAO) Land Cover Classification System [38]. This dataset is based on MODIS MCD43A4 and MCD43A2 from Nasa's Terra and Aqua satellites, using a nadir bidirectional reflectance distribution function at 500 m resolution. Land cover is extrapolated from this data with the help of training sites from across the globe where land cover is fairly stable through time in a sufficiently large region (Figure 3). This allows for the creation of decision trees that account for annually updated global metrics and changing spectral indices for the classification of all other sites [16, 39]. Given the fluctuations that can occur within a region, it is not intended for use as a time series but can be highly useful when representing a change in proportion by comparing two snapshots. This material was selected due to its spatial contiguity and its integrability with the other datasets.

Figure 3: Above, test sites for MODIS MCF12Q1v061 are shown, with many sites located in the boreal forest. The contiguous LCCS1 classification below provides land cover type. Source: [37]

3. Methods

3.1. Fire Selection

I first selected fires from the National Fire Database that aligned with the objective and given datasets. Since Zhang's CSIF product [48] spanned from 2000 to 2020 and likely had greater accuracy towards the later years while the severity product covered up to 2015, the analysis focuses on the most recent years. Simultaneously, it would be necessary to include years before and after the observed fires to determine trends in SIF and examine the recovery.

The fire selection was limited by the size of the CSIF grid cells, which at $0.5^\circ \times 0.5^\circ$ covered roughly 250,000 ha – a very large area compared to the average fire size of 250 ha [27]. I thus chose fires that were likely to be large enough such that changes in SIF could be observed at a grid level.

Filtering out the largest fires ($>100,000$ ha) between 2010-2015 returned 27 fires. While an initial concern had also been the duration of fires given the monthly resolution that I had chosen to work with, every fire burnt for a sufficiently long period, which is typical for fires of such size. Since the Canadian National Fire Database also contains location information, I could determine that all of these fires lie within the boreal forest, both in managed and unmanaged lands.

A defining filtering step came later in the analysis after an initial plotting of severity against SIF recovery. While most fires showcased a severity of 400-600 dNBR

and some fluctuation of recovery rates with occasional decreases likely influenced by drier post-fire years, the three fires with a severity above 650 had significant “second dips”, meaning they had recovery years that were more than 30% below previous years. A closer examination revealed their decreases in SIF were almost negligible compared to other analyzed fires, which artificially inflated their recovery rates, but also made second dips more likely. The same applied to fires 15LX-SENYK and SLK35 with severities between 600 and 650 dNBR, which would have challenged a linear modeling approach. I filtered out these five fires, as they may have been split between grid cells, reducing their signal strength.

Finally, I removed an extreme severity outlier nearly 100 dNBR units below the second-least severe fire. This left 21 fires across Canada between 2010 and 2015. All final selection fires then fell into the moderate-high severity range (440-659 dNBR), the most common range for fires in summer months according to Guindon's 30-year analysis of severity [17].

3.2. SIF Time Series for each fire

To create time series of SIF recovery for each fire, I first had to compile values for a sensible recovery time-frame that would align with the fire areas. Given a multi-year post fire observation was possible with the CSIF dataset, monthly recovery rates would allow for sufficient observation. I thus created monthly averages for all months using nc-formatted CSIF files. Working with xarray, netcdf and rasterio python libraries, I saved a series of monthly gridded mean maps as TIF files which could then be used for further analysis with the CNFDB. I ensured that each file had the same data point corners. Since the magnitude of SIF was only sufficiently large enough within the summer months of the growing season (June-August) (Figure 4), I chose to observe only these months for recovery. Before analyzing the monthly gridded means within the fire areas, the coordinate reference systems had to be aligned. This involved reprojecting all mean TIFs to align with the projection of the fire shapefiles provided in the Canadian National Fire Database (CNFDB). By also using pandas and geopandas libraries, I could then run the rasterstats zonalstats function from the rasterio library, matching the shapefiles of the CNFDB with the information in monthly tifs, and producing SIF time series for each fire and month.

I could then plot a time series with the mean SIFs for each fire area for 2005-2020. The lower magnitude in SIF outside of the summer months was reaffirmed, with recoveries and drops in SIF far less visible from September to May compared to the summer months June to August. To work with just the summer months, I averaged their SIF, creating yearly SIF recovery values for each fire. This gave a growing season average SIF, enabling the creation of a 5-year pre-fire average since all fires had enough years before the fire year, and would

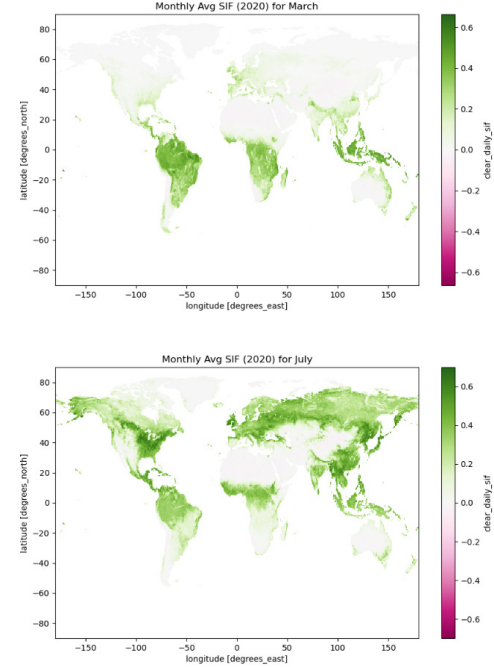


Figure 4: Monthly Mean SIF from CSIF clear-daily product [48] in March vs. July. Units in $\text{mW m}^{-2} \text{nm}^{-1} \text{sr}^{-1}$. The SIF signal is strongest in the growing season observed in the analysis.

allow the observation of the SIF drop from pre-fire to the post-fire minimum (Figure 5). Fires that begin later in the season only showcase their effects in the next year, so I subtracted the minimum SIF of either the fire-year or the post-fire year from the pre-fire average when calculating the SIF drop.

Crucially, this enabled the quantification of recovery rates to pre-fire carbon uptake levels which were a core research focus. Recovery to e-folding heights was also observed, but later deemed of negligible significance, returning no additional information compared to pre-fire average recovery. To account for fluctuations that affected all fires simultaneously, such as large-scale weather events or insect plagues, I conducted a normalization with the average of all 27 unfiltered fires. Since this had a negligible effect on the recovery rates, leaving most unchanged, normalization was excluded from later analysis.

After creating a SIF time series and dataframe with recovery rates to the pre-fire average for each fire and post-fire year, I read in both the created recovery dataframe and the severity data and used the pandas merge function to combine them by their unique fire IDs. Knowing how recovery rates behave compared to pre-fire levels for each fire and having fire severity, I could then plot fire SIF recovery as a result of severity with scatterplots and seaborn regressions.

3.3. Land Cover

To determine the relationship between GPP and fire severity, however, the SIF time series would have to be

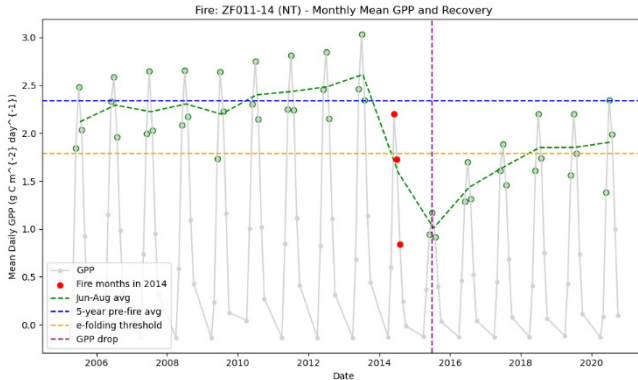


Figure 5: SIF time series for growing season months of ZF011-14 fire (Northwestern Territories). Fire year 2014, SIF drop between 5-year pre-fire average and post-fire minimum in 2015 labeled in purple. Recovery to pre-fire average saved as csv for further analysis. In brown, the average for all 27 fires larger than 100,000 ha is listed to visually observe occurrence of hyperregional phenomena that could have skewed recovery rates. A normalization attempt with this average was conducted.

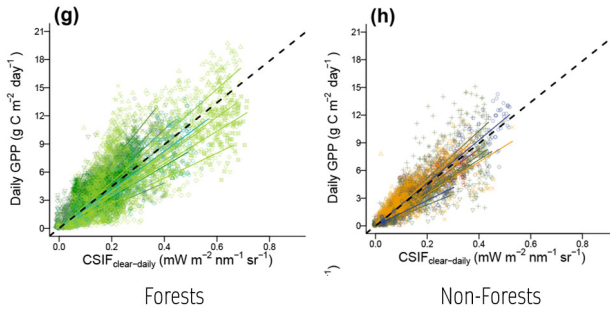
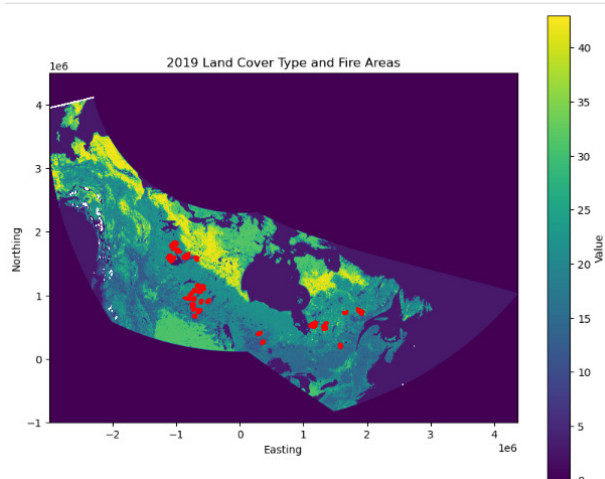


Figure 6: Adopted from Zhang (2018): Clear-sky condition SIF-GPP relationship slopes. GPP/CSIF has a steeper slope for forests than for nonforests.

scaled to GPP. While GPP and SIF are linearly related, this relationship is subject to fluctuation, depending on the land cover type of the observed area [48]. Different vegetation types have different relationships between GPP and SIF measurability depending on plant physiology and photosynthetic efficiencies, causing different slopes when plotted over each other [23]. In figure 6, this difference is depicted, with forests typically having a greater slope than shrubby or grassy non-forest areas.

To find the proportion of land cover in an area, I stitched together the MODIS land cover HDF granules [38] with pyhdf and rasterio libraries such that all of Canada's boreal forest would be covered. After reprojecting this now contiguous mosaic to the fire shapefile coordinate reference system, I could crop it to the fire areas. I then ran another rasterio zonalstats operation, using the land cover type over the fire areas shapefile to determine land cover proportion before and after fires. Figure 7 showcases land cover types across Canada and the fire areas analyzed.

For a snapshot of land cover type proportion before and after fires, I then chose the years 2009 and 2019 and plotted the average land cover for all fires ($n=27$), in-



Name	Value	Description
Barren	1	At least of area 60% is non-vegetated barren (sand, rock, soil) or permanent snow/ice with less than 10% vegetation.
Permanent Snow and Ice	2	At least of area 60% is covered by snow and ice for at least 10 months of the year.
Water Bodies	3	At least 60% of area is covered by permanent water bodies.
Evergreen Needleleaf Forests	11	Dominated by evergreen conifer trees (>2m). Tree cover >60%.
Evergreen Broadleaf Forests	12	Dominated by evergreen broadleaf and palmate trees (>2m). Tree cover >60%.
Deciduous Needleleaf Forests	13	Dominated by deciduous needleleaf (larch) trees (>2m). Tree cover >60%.
Deciduous Broadleaf Forests	14	Dominated by deciduous broadleaf trees (>2m). Tree cover >60%.
Mixed Broadleaf/Needleleaf Forests	15	Co-dominated (40-60%) by broadleaf deciduous and evergreen needleleaf tree (>2m) types. Tree cover >60%.
Mixed Broadleaf Evergreen/Deciduous Forests	16	Co-dominated (40-60%) by broadleaf evergreen and deciduous tree (>2m) types. Tree cover >60%.
Open Forests	21	Tree cover 30-60% (canopy >2m).
Sparse Forests	22	Tree cover 10-30% (canopy >2m).
Dense Herbaceous	31	Dominated by herbaceous annuals (<2m) at least 60% cover.
Sparse Herbaceous	32	Dominated by herbaceous annuals (<2m) 10-60% cover.
Dense Shrublands	41	Dominated by woody perennials (1-2m) >60% cover.
Shrubland/Grassland Mosaics	42	Dominated by woody perennials (1-2m) 10-60% cover with dense herbaceous annual understory.
Sparse Shrublands	43	Dominated by woody perennials (1-2m) 10-60% cover with minimal herbaceous understory.
Unclassified	255	Has not received a map label because of missing inputs.

Figure 7: Map of MODIS MCD12Q1 LCCS1 Land Cover Type classification which is based on the FAO land cover type designation in the bottom part of the figure. Observed fire areas highlighted in red. Data and table retrieved from Sulla-Menashe & Friedl (2022).

cluding the 6 not analyzed for their changes in SIF under the assumption that their land cover change would still be relevant. This returned an interesting change in land cover, but more importantly, proportions that could be used for later analysis. Figure 8 showcases the proportion in land cover, excluding unidentified land covers. Before the fires, the fire areas were covered mostly in Evergreen Needleleaf Forests (ENF), ranging from 10% to >60% tree cover. While the FAO land cover classification does not specify the biome type at a lower density tree cover, it is reasonable to assume that the canopy identified as sparse forests is also evergreen [39]. There are little to no non-forest land cover types. After the fires, the decrease in 30-60% and >60% ENF forest land cover type is the most severe. There is a slight increase in sparse forests and the proportion of non-forest land cover types has risen sharply with dense herbaceous and shrubland grassland mosaics replacing ENF forest. Some of the land is also identified as barren, 4 years after the latest fires in 2015.

These proportions can be used to approximate land

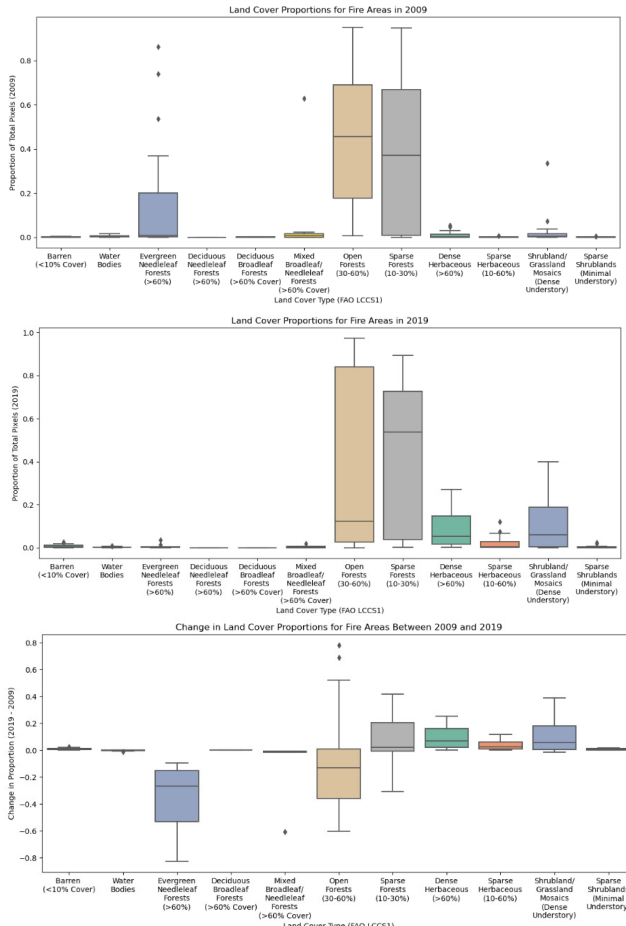


Figure 8: Land cover proportions over fire areas using FAO LCCS classification from MCD12Q1 [39]. Shown are proportions in 2009, 2019, and their difference.

cover types before and after the fire, aligning with slope values provided in previous research. [48] reviewed the relationship between gross primary productivity (GPP) and CSIF by compiling slope regressions from the past two decades. Reported regression slopes between GPP and CSIF ranged from 11.37 to 62.75 ($\text{g C m}^{-2} \text{ day}^{-1}/\text{mW m}^{-2} \text{ nm}^{-1} \text{ sr}^{-1}$) for the CSIF_{clear-daily} product used in this study.

To align the MCD12Q1 land cover classifications with the slopes reported by Zhang, certain categories were approximated, as shown in Figure 9. Zhang derived the SIF-GPP relationship using 42 test sites across distinct land cover types. Based on post-fire land cover data, the FAO LCCS classes were matched with corresponding classes used by Zhang. The fire-affected area was primarily evergreen needleleaf forest (ENF), associated with a slope of approximately 27 ($\text{g C m}^{-2} \text{ day}^{-1}/\text{mW m}^{-2} \text{ nm}^{-1} \text{ sr}^{-1}$), while areas with sparser forest cover typically exhibit lower slope values.

For the average of the fire areas, I then calculated a weighted average of slopes based on the land cover type proportion, leaving pre- and post-fire slopes of 25.2 and 24.4 $\text{g C m}^{-2} \text{ d}^{-1}/\text{mW m}^{-2} \text{ nm}^{-1} \text{ sr}^{-1}$ respectively. Using these slope coefficients then allows for a scaling of SIF

GPP/CSIF-Slopes by Land Cover Type in $\text{g C m}^{-2} \text{ d}^{-1}/\text{mW m}^{-2} \text{ nm}^{-1} \text{ sr}^{-1}$

- 11: Evergreen Needleleaf Forests: 27
- 21: Open Forests (~WSA): 27
- 22: Sparse Forests (~SAV): 20
- 31: Dense Herbaceous (~CSH): 15
- 32: Sparse Herbaceous (~OSH): 28
- 41: Shrubland/Grassland Mosaics (~avg of OSH, GRA): 24
- 42: Sparse Shrublands (~OSH): 28

Figure 9: GPP/CSIF slopes adopted from Zhang and adjusted for land cover type differences between Zhang's [48] classification in parentheses and the FAO LCCS1 classification used by Sulla-Menache & Friedl [39] after the colon. While Zhang did not include uncertainties, these are rounded to two significant figures. Abbreviations are as follows: ENF, evergreen needleleaf forest; EBF, evergreen broadleaf forest; DNF, deciduous needleleaf forest; DBF, deciduous broadleaf forest; MF, mixed forest; CSH, closed shrubland; OSH, open shrubland; WSA, woody savannas; SAV, savannas; GRA, grassland; WET, wetland; CRO, cropland; URB, urban; CNV, crop-land or natural vegetation mosaics.

before and after the fires.

3.4. GPP Time Series

The scaling of the SIF/severity time series to a GPP/severity time series multiplied each growing season average SIF value up to the fire year with the pre-fire slope and each SIF value after the fires with the post-fire slope. This returned a GPP time series (Figure 10) and data frame with recovery rates to the pre-fire GPP average for each fire and post-fire year, which were once again merged with severity data for later analysis.

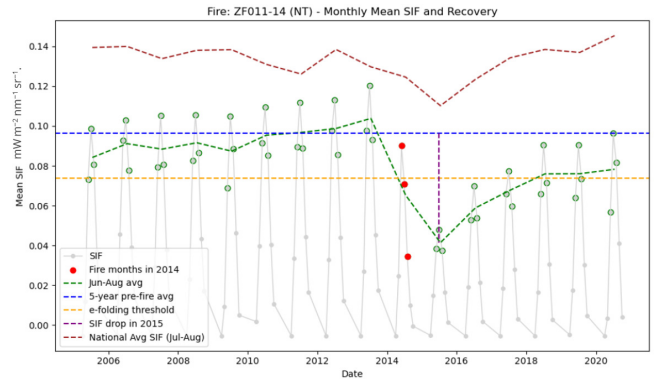


Figure 10: GPP time series for growing season months of ZF011-14 fire (Northwestern Territories). Fire year 2014 in red, GPP drop between 5-year pre-fire average and post-fire minimum in 2015 along vertical purple line. Recovery to pre-fire average saved as csv for further analysis.

4. Results

4.1. SIF & Fire Severity

I first graphed the recovery for each year individually. To better visualize the full relationship for all years, I included all regressions in one graph with progressively darker regression lines for each year. The average recovery rate is increasing year

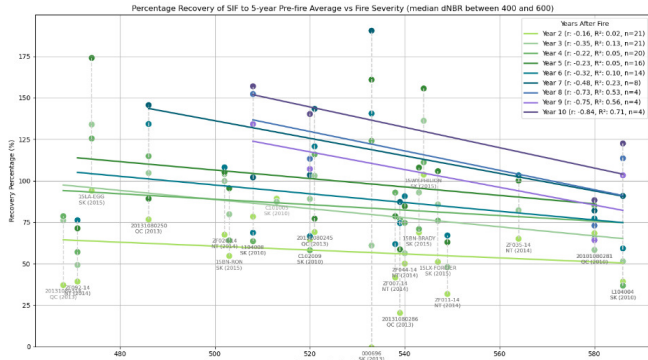


Figure 11: SIF recovery rates from the second to tenth year post-fire as long as data exists. The percentage is given as percentage of recovery to the 5-year pre-fire average level of SIF. A negative correlation coefficient indicates an inverse relationship across all years. All fires are labeled by name.

over year with regressions of later years lying further away along the recovery percentage axis. Each year showcases a negative correlation coefficient between recovery percentage and fire severity. This suggests a weak inverse relationship. Figure 11 showcases these results in a compact manner. The weighted average of the coefficients until year 7 is $r=-0.27$ (ranging from $r=-0.16$ to $r=-0.48$). This excludes the years 8 through 10, for which there were just 4 fires.

4.2. GPP & Fire Severity

With scaled GPP and recovery percentages, I also plotted recovery rates over fire severity. As with the SIF relationship, the average GPP recovery rate increases year over year, with each year also having a negative correlation coefficient between recovery percentage and fire severity. This suggests a weak inverse relationship. Figure 12 showcases the full range of GPP to severity results. The weighted average of the coefficients until year 7 is $r=-0.27$ (ranging from $r=-0.14$ to $r=-0.53$). This again excludes the years 8 through 10, for which there were just 4 fires.

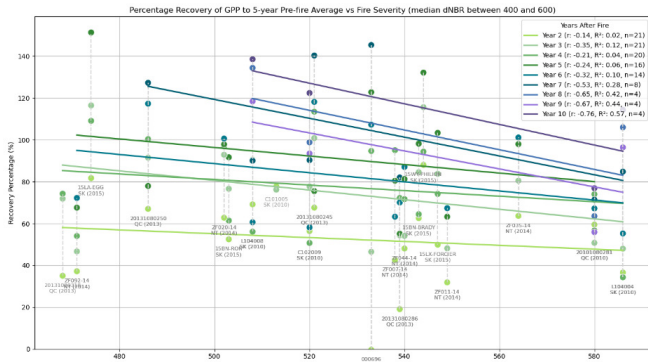


Figure 12: Linearly scaled GPP recovery rates from the second to tenth year post-fire as long as data exists. The percentage is given as percentage of recovery to the 5-year pre-fire average level of GPP.

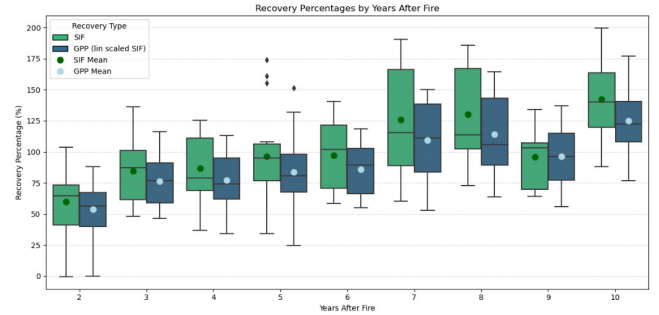


Figure 13: SIF and GPP recovery rates from second to tenth year post-fire as long as data exists. Percentage is given as percentage of recovery to 5-year pre-fire average level of GPP/SIF. Boxplots represent the median and interquartile range of recovery percentages while mean recovery values are overlaid with round markers. Any outliers are shown as individual points above the boxplots.

4.3. SIF/GPP Recovery

I then averaged the recovery rates for each year – both in terms of SIF and GPP. The boxplot in figure 13 showcases this relationship, with GPP recovery rates lagging behind the SIF recovery rates. Mean recovery rates are included in dots. SIF takes on average 6 years to recover back to pre-fire levels, while GPP recovers in closer to 7 years.

Both SIF and GPP rates overshoot pre-fire levels 7 years after the fire. For years 8, 9, and 10 the sample size is fairly small – consisting only of four fires from 2010. The overshoot continues, aside from a slight dip in year 9.

5. Discussion and Limitations

5.1. Fire Selection and Dataset Constraints

I removed several fires from the analyzed dataset due to them being severity outliers and having insignificant SIF drops. Including these fires led to a slightly positive linear relationship – contrary to the opposite finding. With a clearly negative trend among the moderate severity fires but a slight positive trend among the 5 highest severity fires when including all 27 fires, a linear fit suggested higher severity fires might lead to more rapid recoveries. This finding exacerbates the ambiguity of the findings – a tendency reflected in previous research [34].

Ambiguities could be minimized and the need for filtering reduced with either a non-linear model or by examining a broader range of fires. The coarse resolution of the CSIF dataset [48] was chosen to accommodate low computing power and was the only publicly available product of comparable contiguity. But this resolution constrained the selection of fires to a small number of very large fires ($> 100,000$ ha) to ensure they would be included in each grid cell. Even then, fires wouldn't cover pixels fully, leading to diminished signals depending on coverage, further increasing ambiguity. Drawing on a different dataset, such as Zhang's 0.05° resolution CSIF product available upon request, would allow the

targeting of a broader range of fires. The inclusion of fires could then be controlled to strong signals only by calculating the proportion of each grid cell covered by a fire and allowing the analysis to focus only on grid cells that meet a certain fire proportion threshold.

Another source of uncertainty in recovery rates stems from the low quantity of fires with more than 5 years recovery time. Since only fires from 2010-2015 were selected for examination with the CSIF dataset that spanned 2000-2020, all fires could be used to report recovery rates in the first five years after the fire, but only fires in 2010 would have 10 years of post-fire succession. Shifting to a period of 2005 to 2012 instead would allow the inclusion of a greater number of fires with a 5-year pre-fire average and more fires with a longer succession period of 7-15 years. Out of the 21 fires examined between 2010 and 2015, only 13 recovered fully.

Ambiguities could also be quantified by determining the statistical significance. Regardless of data, fire selection, and modeling alternatives, the outlier treatment and the fire selection significantly impacted the quality of the findings and thus begs re-examination.

5.2. Severity/SIF relationship

Given that large fires, such as the ones selected here tend to be patchier and have patches of greater size [7] – leaving unburned islands neighboring large severely burned forest stands – it was important to consider the median dNBR for each fire. I wanted to determine whether dNBR severity and CSIF drops would be similar, since dNBR uses Landsat NDVI while CSIF is using MODIS input data for 4 bands that better approximates SIF, but still partially relies on reflectance-based input data. Interestingly, SIF drop and median dNBR were positively correlated for the core fire group (Figure 14). Selecting a severity product that doesn't

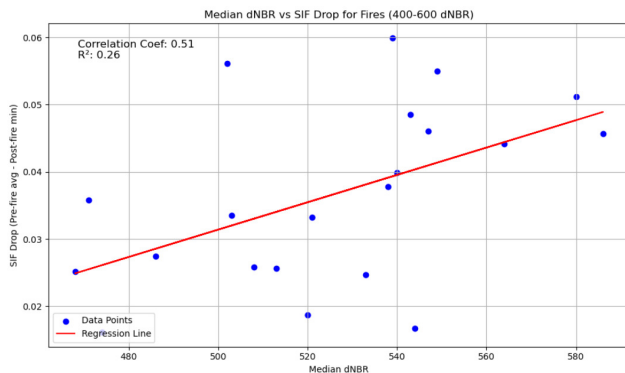


Figure 14: Positive relationship between SIF drop and median dNBR visualized

depend on any reflectance-based measurements might find a weaker positive relationship. I also examined the relationship of fire size and SIF recovery rates and found a correlation coefficient near zero – which aligned with Guindon's recent analysis of severities from 1985-2015 [17], although earlier studies indicated a positive relationship between fire size and severity [42].

5.3. GPP/SIF relationship

Land cover estimation relied on multiple averages and the approximation of land cover types to utilize GPP/SIF coefficients discovered by [48]. This and the utilization of relatively large grid cells from the CSIF product likely smoothed over the effects of land cover change on GPP, leading to less significant differences in slope between 2009 and 2019 (Figure 9) than the true difference, which would probably see a GPP recovery that is further delayed and showcases more significant land cover changes. Since land cover was only sporadically explored – yielding greater uncertainty – a more thorough investigation should begin with an analysis of land cover by individual fire. Post-fire SIF recovery dynamics have been examined previously in relation to land cover, most recently by [23], with ambiguous results reflecting a range of recovery times with a negligible impact on long-term storage capabilities and an increase in seasonality in the short-term. This challenge is present in all land-cover carbon uptake recovery considerations, and motivates this research, but remains to be resolved conclusively. It should also be noted that land cover was constructed using MODIS MCD43A4 and A2 measurements while the CSIF dataset relied on MODIS MCD43C4 which could risk some degree of shared reflectance input data. Overall, land cover estimation and slopes between SIF and GPP are more accurate than NDVI approaches but remain approximate in relation to direct GPP measurements using flux towers. In the trade-off between accuracy and spatial resolution, the benefits of satellite SIF measurements outweigh.

5.4. Uncertainty and Contextual Drivers

I did not conduct an uncertainty estimation. Uncertainties also were not reported for Zhang's CSIF dataset [48] nor the CanLaBS severity product [17]. However, the greatest uncertainties were likely not derived from the accessed datasets but instead compounded through multi-step processes in the utilized methods such as the averaging of slopes in the land cover analysis. Uncertainty could also stem from confounding factors skewing recovery rates, such as insect infestation, droughts, or rainier summers. Canada tracks these under land-based disturbances, but wildfire fluxes are the single most significant cause of emissions with insect emissions on steady decline since 2008 [11].

Another important consideration to make is the geographical clustering on varying scales. Recovery rates could have been linked to severity through confounding variables such as ecological drivers, rainfall rates, or the El Niño-Southern Oscillation. While using a greater number of fires could avoid this issue, a statistical analysis for confounding variables should be conducted to determine their impact and significance. Human activity should also be considered. Whether a fire occurred on managed or unmanaged lands might

also have impacted recovery rates, depending on logging rates and whether there was an effort to suppress the fires or replant post-fire.

I also considered factors that could have affected fires regionally in the examined fire years. For fires with a noticeable second dip, I examined events and discovered noticeable fluctuations in 2015 and 2019. The 2019 dip coincides with the SIF/GPP dip in year 9 for the 2010 fires – the only fires with a 9th year of data. Historic data revealed droughts in Western Canada in 2015 as a result of an extreme El Niño year, and a drier spring followed by extreme rainfall in the prairies in 2019 as a result of a weaker El Niño [41, 10]

5.5. Implications and Future Research

The results showcase a slightly negative relationship between recovery rates and fire severity and suggest more severe fires make forests recover more slowly in the first years after a fire. It also identifies GPP recoveries to be slightly slower than SIF recoveries due to lower scaling factors for non-forested compared to forested areas.

Recovery times of 6 to 7 years discovered in this work are faster than previous research suggests. Several previous studies were carried out in boreal forest ecosystems with optical sensors, which found a mean post-fire NPP recovery for North American boreal forests of about 9 years with NDVI measurements and 13 years for the Siberian boreal counterparts using NDVI and NDSWIR (normalized difference shortwave infrared index) reflectance [24]. Researchers examining the overall change in post-fire signal recovery found Canadian forest NBR recoveries to have increased by 18% in the Taiga Shield East and 9% in the Taiga Shield, while changes in boreal forest recovery rates were ambiguous from 1986-2011 and depended on the ratio of climate change induced warming and lack of moisture [15]. This could suggest that the exceptionally large fires I selected tend to have faster signal recovery than the fires analyzed by other researchers. It could also suggest that SIF-based recovery rates are more rapid than previous vegetation-index recoveries.

The negative relationship between SIF/GPP recovery and severity within the first 10 years after fires aligns with previous research for coniferous areas using reflectance-based indices. [34] identified a slightly faster recovery for high severity fires in California between 2001 and 2019, reaching parity with lower severity fires by year 7, which might be due to the warmer climate in California. This could also be influenced by their use of a reflectance-based index.

Unexplored uncertainty causes and potentially confounding variables do not diminish the conclusion that databases and methods were appropriate for determining the fire severity and GPP recovery relationship. But increased ambiguity and a weak correlation does beg for a consideration of more fires and more statistically rigorous work. Future research should examine

external disturbances, regional differences, and covariabes such as patchiness or tree cover sparseness, analyze land cover type by fire, explore the utilization of more detailed datasets and emerging sensor information, and examine policy and greenhouse gas accounting implications. Significant improvements could be achieved through a national comparison that examines not just fluctuations in the observed fire areas but across the entire boreal region. Future studies could also examine adjacent regions, such as the Taiga, to further determine how severity and recovery relate under varying land cover types. As remote sensing technology evolves, new datasets should also be considered for use. While Zhang's [48] 0.05° dataset would be a sensible next step, measurements from new satellites, such as TROPOMI (2017) or FLuorescence EXplorer (launching mid-2026), promise a greater resolution of SIF with a 300m grid and 150km swath compared to OCO-2's 2km grid and 10km swath [2]. This will enable better contiguous analysis that won't require the use of any reflectance-based vegetation indices [12]. Future research should also examine the integration of SIF/GPP measurements into national GHG Inventory projections and wildfire management as droughts increase wildfire intensity. Since SIF and products such as CSIF are a better approximator of carbon uptake than NDVI and are especially useful to determine photosynthetic activity in coniferous regions, their integration could be of interest to fire risk mapping in Canada, which currently relies on the Canadian Forest Fire Behavior Prediction System that uses land cover type and NDVI to estimate risk [30].

These steps will be necessary before steadfast conclusions can be drawn regarding carbon uptake. To assist with the holistic evaluation of carbon drawdown after fires, this research could also be integrated with research on net ecosystem exchange.

6. Conclusion

Comparing the recovery of gross primary productivity as a function of fire severity is a crucial step towards understanding the impacts of climate change on global carbon budgets. I discovered that remotely sensed solar-induced fluorescence offers a promising outlook for the study of GPP recovery and severity, identifying two key findings: First, photosynthetic activity in Canada's boreal forests recovers to pre-fire levels in 6 to 7 years after the large fires, with GPP recoveries lagging slightly behind SIF recovery. When accounting for differing SIF/GPP slopes depending on land cover change from forested to non-forested areas, the recovery is slower compared to only examining SIF. This recovery is slightly faster than previous research suggests. Second, both SIF recovery and GPP recovery have weak inverse relationships to fire severity, indicating that the carbon uptake of more severe fires recovers slower in the first ten years post-fire. These findings

are consistent with previous research, although there are studies that showcase the opposite. This is no indication of the duration of overall carbon drawdown or biomass recovery, but it is a decisive step towards a more detailed account of post-fire vegetation-based carbon uptake. While the results aren't entirely conclusive, the outlined methods are replicable, offering a promising insight into the relationship of SIF and fire severity and showcasing the potential of SIF-based products. Ambiguities and uncertainties demand a more detailed consideration of external factors and a more robust statistical methodology, and future studies should consider a greater quantity of fires with a greater range of sizes and severities.

An improved understanding of the impact of fire severity on the boreal carbon cycle can enable more efficient forest management and inform the development of carbon emissions reduction approaches. It is thus imperative that this work is continued due to its significance on global land sinks.

7. Data availability

The following public datasets were used in the analysis.

MODIS land cover data is available from the Land Processes Distributed Active Archive Center (LPDAAC) at the U.S. Geological Survey (USGS) Earth Resources Observation and Science Center (EROS) (<http://lpdaac.usgs.gov>) and the University of Maryland. The specific dataset can be found here: [<https://e4ft101.cr.usgs.gov/MOTA/MCD12Q1.061/>] (<https://e4ft101.cr.usgs.gov/MOTA/MCD12Q1.061/>).

The CSIF dataset with a 0.5° spatial resolution and 4-day temporal resolution, from which I used CSIF_{clear-daily}, can be accessed through Figshare: [<https://doi.org/10.6084/m9.figshare.6387494>] (<https://doi.org/10.6084/m9.figshare.6387494>) [48].

Fire data, including size and location, is available from Canada's National Fire Database: [<https://cwfis.cfs.nrcan.gc.ca/datamart/metadata/nfdbpoly>] (<https://cwfis.cfs.nrcan.gc.ca/datamart/metadata/nfdbpoly>) [29].

The boreal forest shapefile is available from Natural Resources Canada at: [<https://naturalresources.ca/our-natural-resources/forests/sustainable-forest-management/>] (<https://naturalresources.ca/our-natural-resources/forests/sustainable-forest-management/>) borealforest/north-american-boreal-zone-map-shapefiles/14252.

References

- [1] Balshi, M., McGuire, A., Duffy, P., Flannigan, M., Kicklighter, D., & Melillo, J. (2009). Vulnerability of carbon storage in North American boreal forests to wildfires during the 21st century. *Global Change Biology*, *15*, 1491-1510. <https://doi.org.myaccess.library.utoronto.ca/10.1111/j.1365-2486.2009.01877.x>
- [2] Bacoü, C., Maignan, F., Peylin, P., MacBean, N., Bastrikov, V., Joiner, J., ... Frankenberg, C. (2019). Differences Between OCO-2 and GOME-2 SIF Products From a Model-Data Fusion Perspective. *Journal of Geophysical Research Biogeosciences*, *124*(10), 3143-3157. <https://doi.org/10.1029/2018jg004938>
- [3] Berry, J. A., Frankenberg, C., & Wennberg, P. (2013). New methods for measurements of photosynthesis from space (Final Report). Keck Institute for Space Studies. https://kiss.caltech.edu/final_reports/Photosynthesis_final_report.pdf
- [4] Byrne, B., Liu, J., Bowman, K.W. et al. (2024). Carbon emissions from the 2023 Canadian wildfires. *Nature* *633*, 835-839. <https://doi.org/10.1038/s41586-024-07878-z>
- [5] Canadian Net-zero Emissions Accountability Act (2021). S.C. 2021, c. 22. <https://laws-lois.justice.gc.ca/eng/acts/c-19.3/fulltext.html>
- [6] Climate Action Tracker. (2024). Canada. <https://climateactiontracker.org/countries/canada/>
- [7] Cova, T. J., Dennison, P. E., Kim, D. H., & Sieg, C. H. (2022). The influence of topography, fuels, and fire weather on fire size and patch mosaic complexity: A simulation study. *Landscape Ecology*, *37*, 1637-1651.
- [8] David Suzuki Foundation. (2019). Position Paper and Technical Summary — Taking Credit: Canada and the Role of Sinks in International Climate Negotiations. <https://davidsuzuki.org/science-learning-centre/article/position-paper-and-technical-summary-taking-credit-canada-and-the-role-of-sinks-in-international-climate-negotiations/>
- [9] Doughty, R., Kurosu, T. P., Parazoo, N., Philipp Köhler, Wang, Y., Sun, Y., & Frankenberg, C. (2022). Global GOSAT, OCO-2, and OCO-3 solar-induced chlorophyll fluorescence datasets. *Earth System Science Data*, *14*(4), 1513-1529. <https://doi.org/10.5194/essd-14-1513-2022>
- [10] Environment and Climate Change Canada. (2019). Canada's top 10 weather stories of 2019 - Canada.ca. <https://www.canada.ca/en/environment-climate-change/services/top-ten-weather-stories/2019.html>
- [11] Environment and Climate Change Canada (2024). Canadian Environmental Sustainability Indicators: Land-based greenhouse gas emissions and removals from natural disturbances. <https://www.canada.ca/en/environment-climate-change/services/environmental-indicators/land-based-greenhouse-gas-emissions-removals.html>
- [12] European Space Agency. (2024). FLEX Mission Summary. ESA CEOS. https://database.eohandbook.com/database/missionsummary.aspx?missionID=836&utm_source=eoportal&utm_content=flex
- [13] Foster, A. C., Wang, J. A., Frost, G. V., Davidson, S. J., Hoy, E., Turner, K. W., ... Du, J. (2022). Disturbances in North American boreal forest and Arctic tundra: impacts, interactions, and responses. *Environmental Research Letters*, *17*(11), 113001-113001. <https://doi.org/10.1088/1748-9326/ac98d7>
- [14] Frankenberg, C., Fisher, J. B., Worden, J., Badgley, G., Saatchi, S. S., Lee, J.-E., ... Yokota, T. (2011). New global observations of the terrestrial carbon cycle from GOSAT: Patterns of plant fluorescence with gross primary productivity. *Geophysical Research Letters*, *38*(17). <https://doi.org/10.1029/2011gl048738>
- [15] Frazier, R. J., Coops, N. C., Wulder, M. A., Hermosilla, T., & White, J. C. (2017). Analyzing spatial and temporal variability in short-term rates of post-fire vegetation return from Landsat time series. *Remote Sensing of Environment*, *205*, 32-45. <https://doi.org/10.1016/j.rse.2017.11.007>
- [16] Friedl, M. A., Sulla-Menashe, D., Tan, B., Schneider, A., Ramanukutty, N., Sibley, A., & Huang, X. (2010). MODIS Collection 5 global land cover: Algorithm refinements and characterization of new datasets. *Remote Sensing of Environment*, *114*(1), 168-182. <https://doi.org/10.1016/j.rse.2009.08.016>
- [17] Guindon, L., Gauthier, S., Manka, F., Parisien, M.-A., Whitman, E., Bernier, P., Beaudoin, A., Villemaire, P., & Skakun, R. (2020). Trends in wildfire burn severity across Canada, 1985 to 2015. *Canadian Journal of Forest Research*, *51*(9), 1230-1244. <https://doi.org/10.1139/cjfr-2020-0353>
- [18] Hemes, K. S., Norlen, C. A., Wang, J. A., Goulden, M. L., & Field, C. B. (2023). The magnitude and pace of photosynthetic recovery after wildfire in California ecosystems. *Proceedings of the National Academy of Sciences*, *120*(15). <https://doi.org/10.1073/pnas.2201954120>
- [19] Joiner, J., Yoshida, Y., Vasilkov, A.P., Schaefer, K., Jung, M., Guanter, L., ... Marchesini, L. B. (2014). The seasonal cycle of

- satellite chlorophyll fluorescence observations and its relationship to vegetation phenology and ecosystem atmosphere carbon exchange. *Remote Sensing of Environment*, 152, 375–391. <https://doi.org/10.1016/j.rse.2014.06.022>
- [20] Jones, M. W., Santín, C., van, & Doerr, S. H. (2019). Global fire emissions buffered by the production of pyrogenic carbon. *Nature Geoscience*, 12(9), 742–747. <https://doi.org/10.1038/s41561-019-0403-x>
- [21] Ke, P., Ciais, P., Sitch, S., Li, W., Bastos, A., Liu, Z., ... Chevallier, F. (2024). Low latency carbon budget analysis reveals a large decline of the land carbon sink in 2023. *National Science Review*. <https://doi.org/10.1093/nsr/nwae367>
- [22] Keenan, T. F., Luo, X., Stocker, B. D., De, G., Medlyn, B. E., Prentice, I. C., ... Zhou, S. (2023). A constraint on historic growth in global photosynthesis due to rising CO₂. *Nature Climate Change*, 13(12), 1376–1381. <https://doi.org/10.1038/s41558-023-01867-2>
- [23] Kim, J. E., Wang, J. A., Li, Y., Czimczik, C. I., & Rutherford, J. T. (2024). Wildfire-induced increases in photosynthesis in boreal forest ecosystems of North America. *Global Change Biology*, 30(1). <https://doi.org/10.1111/gcb.17151>
- [24] Kurbanov, E., Vorobev, O., Lezhnin, S., Sha, J., Wang, J., Li, X., ... Wang, Y. (2022). Remote Sensing of Forest Burnt Area, Burn Severity, and Post-Fire Recovery: A Review. *Remote Sensing*, 14(19), 4714. <https://doi.org/10.3390/rs14194714>
- [25] McCullum, A. J., Torres-Pérez, J. L. (2022). Using Earth Observations for Pre- and Post-Fire Monitoring. *NASA's Applied Remote Sensing Training Program*. Retrieved from https://appliedsciences.nasa.gov/sites/default/files/2022-01/Advanced_Fires_2022_Part2_Final_Edited_SC.pdf
- [26] Natural Resources Canada I (2024). Canada's record-breaking wildfires in 2023: A fiery wake-up call. <https://natural-resources.canada.ca/simply-science/canadas-record-breaking-wildfires-2023-fiery-wake-call/25303>
- [27] Natural Resources Canada II (2024). boreal forest. <https://natural-resources.canada.ca/our-natural-resources/forests/sustainable-forest-management/boreal-forest/13071>
- [28] Natural Resources Canada III (2024). Canadian Wildland Fire Information System — Metadata. <https://cwfis.cfs.nrcan.gc.ca/datamart/metadata/nfdbpnt>
- [29] Natural Resources Canada IV. (2024). Canadian Wildland Fire Information System — CWFIS Datamart. <https://cwfis.cfs.nrcan.gc.ca/datamart>
- [30] Natural Resources Canada V. (2020). Satellite/NDVI data for CWFIS/fire danger rating in Canada. https://cwfis.cfs.nrcan.gc.ca/downloads/pcuring/Satellite_NDVI_data_for_CWFIS_fire_danger_rating_in_Canada.pdf
- [31] NASA Jet Propulsion Laboratory. (n.d.). OCO-2 Data Center. <https://oco2.jpl.nasa.gov/science/oco-2-data-center/>
- [32] Pickering, M., Cescatti, A., & Duveiller, G. (2022). Sun-induced fluorescence as a proxy for primary productivity across vegetation types and climates. *Biogeosciences*, 19(20), 4833–4864. <https://doi.org/10.5194/bg-19-4833-2022>
- [33] Pleniou, M., & Koutsias, N. (2013). Sensitivity of spectral reflectance values to different burn and vegetation ratios: A multi-scale approach applied in a fire affected area. *ISPRS Journal of Photogrammetry and Remote Sensing*, 79, 199–210. <https://doi.org/10.1016/j.isprsjprs.2013.02.016>
- [34] Qiu, L., Fan, L., Sun, L., Zeng, Z., Feng, L., Yue, C., & Zheng, C. (2023). Higher burn severity stimulates post-fire vegetation and carbon recovery in California. *Agricultural and Forest Meteorology*, 342, 109750–109750. <https://doi.org/10.1016/j.agrmet.2023.109750>
- [35] Ramos Fjellvang, C. (n.d.). Why did Canada withdraw from the Kyoto Protocol? A case study. Retrieved from <https://www.fni.no/getfile.php/131693-1469868970/Filer/Publikasjoner/FNI-R0115.pdf>
- [36] Smyth, C., Metsaranta, J., Fortin, M., Le Noble, S., MacDonald, H., Wolfe, J., et al. (2023). Blueprint for forest carbon science in Canada. Government of Canada, Natural Resources Canada. https://publications.gc.ca/collections/collection_2024/rncan-nrcan/Fo4-43-2024-eng.pdf
- [37] Sulla-Menashe, D., Gray, J. M., Abercrombie, S. P., Friedl, M. A. (2019). Hierarchical mapping of annual global land cover 2001 to present: The MODIS Collection 6 Land Cover product. *Remote Sensing of Environment*. <https://doi.org/10.1016/j.rse.2018.12.013>
- [38] Sulla-Menashe, D., & Friedl, M. (2022). MCD12Q1. Land Processes Distributed Active Archive Center. <https://lpdaac.usgs.gov/products/mcd12q1v061/>
- [39] Sulla-Menashe, D., & Friedl, M. (2022). MODIS Collection 6.1 (C61) Land Cover Type Product User Guide. Land Processes Distributed Active Archive Center. https://lpdaac.usgs.gov/documents/1409/MCD12_User_Guide_V61.pdf
- [40] Sun, Y., Frankenberg, C., Jung, M., Joiner, J., Guanter, L., Philipp Köhler, & Magney, T. (2018). Overview of Solar-Induced chlorophyll Fluorescence (SIF) from the Orbiting Carbon Observatory-2: Retrieval, cross-mission comparison, and global monitoring for GPP. *Remote Sensing of Environment*, 209, 808–823. <https://doi.org/10.1016/j.rse.2018.02.016>
- [41] Szeto, K., Zhang, X., White, R. E., & Brimelow, J. (2016). The 2015 Extreme Drought in Western Canada. *Bulletin of the American Meteorological Society*, 97(12), S42–S46. <https://doi.org/10.1175/bams-d-16-0147.1>
- [42] Turetsky, M. R., Kane, E. S., Harden, J. W., Ottmar, R. D., Manies, K. L., Hoy, E., amp; Kasischke, E. S. (2011). Recent acceleration of biomass burning and carbon losses in Alaskan forests and peatlands. *Nature Geoscience*, 4(1), 27–31. <https://doi.org/10.1038/ngeo1027>
- [43] UNFCCC (2015). Part two: Action taken by the Conference of the Parties at its twenty-first session. In: Report of the Conference of the Parties on its twenty-first session, held in Paris from 30 November to 13 December 2015. <https://unfccc.int/documents/9097>
- [44] UNFCCC. (2021). Canada's 2021 Nationally Determined Contribution under The Paris Agreement. https://unfccc.int/sites/default/files/NDC/2022-06/Canada's%20Enhanced%20NDC%20Submission1_FINAL%20EN.pdf
- [45] UN-SPIDER. (n.d.). Spectral responses of healthy vegetation and burned areas. https://un-spider.org/sites/default/files/Spectral_responses.jpg
- [46] Wang, Z., Wang, Z., Zou, Z., Chen, X., Wu, H., Wang, W., ... Zhu, J. (2023). Severe Global Environmental Issues Caused by Canada's Record-Breaking Wildfires in 2023. *Advances in Atmospheric Sciences*, 41(4), 565–571. <https://doi.org/10.1007/s00376-023-3241-0>
- [47] Wu, D., Lin, J. C., Duarte, H. F., Yadav, V., Parazoo, N. C., Oda, T., amp; Kort, E. A. (2021). A model for urban biogenic CO₂ fluxes: Solar-Induced Fluorescence for Modeling Urban biogenic Fluxes (SMURF v1). *Geoscientific Model Development*, 14(6), 3633–3661. <https://doi.org/10.5194/gmd-14-3633-2021>
- [48] Zhang, Y., Joiner, J., Seyed Hamed Alemohammad, Zhou, S., amp; Gen2ne, P. (2018). A global spatially contiguous solar-induced fluorescence (CSIF) dataset using neural networks. *Biogeosciences*, 15(19), 5779–5800. <https://doi.org/10.5194/bg-15-5779-2018>
- [49] Zheng, Y., Shen, R., Wang, Y., Li, X., Liu, S., Liang, S., ... Yuan, W. (2020). Improved estimate of global gross primary production for reproducing its long-term variation, 1982–2017. *Earth System Science Data*, 12(4), 2725–2746. <https://doi.org/10.5194/essd-12-2725-2020>